Original Article

MOLECULAR METABOLISM

Ablation of glucokinase-expressing tanycytes impacts energy balance and increases adiposity in mice

Antoine Rohrbach [1,2], Emilie Caron [3], Rafik Dali [2], Maxime Brunner [4], Roxane Pasquettaz [1], Irina Kolotuev [5], Federico Santoni [4], Bernard Thorens [1], Fanny Langlet [1,2,*]

ABSTRACT

Objectives: Glucokinase (GCK) is critical for glucosensing. In rats, GCK is expressed in hypothalamic tanycytes and appears to play an essential role in feeding behavior. In this study, we investigated the distribution of GCK-expressing tanycytes in mice and their role in the regulation of energy balance.

Methods: *In situ* hybridization, reporter gene assay, and immunohistochemistry were used to assess GCK expression along the third ventricle in mice. To evaluate the impact of GCK-expressing tanycytes on arcuate neuron function and mouse physiology, *Gck* deletion along the ventricle was achieved using loxP/Cre recombinase technology in adult mice.

Results: GCK expression was low along the third ventricle, but detectable in tanycytes facing the ventromedial arcuate nucleus from *bregma* −1.5 to −2.2. *Gck* deletion induced the death of this tanycyte subgroup through the activation of the BAD signaling pathway. The ablation of GCK-expressing tanycytes affected different aspects of energy balance, leading to an increase in adiposity in mice. This phenotype was systematically associated with a defect in NPY neuron function. In contrast, the regulation of glucose homeostasis was mostly preserved, except for glucoprivic responses.

Conclusions: This study describes the role of GCK in tanycyte biology and highlights the impact of tanycyte loss on the regulation of energy balance.

Keywords Glucokinase; Tanycytes; Energy balance; Glucose homeostasis; Apoptosis; Hypothalamus

1. INTRODUCTION

The maintenance of energy balance and glucose homeostasis is orchestrated by specialized neural cells organized in networks that connect the hypothalamus and the brainstem [1]. The reliability of this regulatory system is contingent on the adequate sensing and integration of metabolic signals, which continuously inform the brain about the fraction of energy that enters (food intake) and leaves (energy expenditure) the organism.

In the hypothalamus, peculiar glial cells called tanycytes are strategically positioned to sense metabolic information [2]. Hypothalamic tanycytes are elongated cells that line the lateral walls and floor of the third ventricle and extend basal processes into nuclei involved in the regulation of energy balance, such as the arcuate nucleus (ARH), the ventromedial nucleus (VMH), and the dorsomedial nucleus (DMH) [3,4]. This polarized shape allows tanycytes to contact different actors within the hypothalamic parenchyma, including the cerebrospinal fluid, blood vessels, and neurons [4,5]. In addition, tanycytes present dynamic gene expression profiles that allow them to detect both central [6] and peripheral metabolic information [3] and to adapt their sensing functions to the physiological demand [7].

Glucokinase (GCK) is considered a key player in tanycyte metabolic sensing, as its deletion or inhibition leads to an alteration in glucose homeostasis and energy balance in rats [8,9]. GCK is a glycolytic enzyme present in various glucose-sensing cells, including pancreatic β cells or hepatocytes [10,11]. This enzyme is involved in numerous cellular processes that range from glycolysis to cell survival [12]. In particular, it plays a pivotal role in cells that face high variations in glucose levels by giving them protection against glucotoxicity [13]. As tanycyte location at the interface between different compartments

[1]Center for Integrative Genomics, Faculty of Biology and Medicine, University of Lausanne, Lausanne, Switzerland [2]Department of Biomedical Sciences, Faculty of Biology and Medicine, University of Lausanne, Lausanne, Switzerland [3]Univ. Lille, Inserm, CHU Lille, Laboratory of Development and Plasticity of the Neuroendocrine Brain, Lille Neuroscience & Cognition, UMR-S, 1172, Lille, France [4]Service of Endocrinology, Diabetology, and Metabolism, Lausanne University Hospital, Faculty of Biology and Medicine, 1011, Lausanne, Switzerland [5]Electron Microscopy Facility, Faculty of Biology and Medicine, University of Lausanne, Lausanne, Switzerland

*Corresponding author. Department of Biomedical Sciences, University of Lausanne, Bugnon 7, 1005, Lausanne, Switzerland. E-mail: fanny.langlet@unil.ch (F. Langlet).

Abbreviations: 2-DG, 2-deoxyglucose; AgRP, agouti-related peptide; ARH, arcuate nucleus; CART, cocaine- and amphetamine-related transcript; DIO2, deiodinase 2; DMH, dorsomedial nucleus; GCK, glucokinase; ME, median eminence; NPY, neuropeptide Y; POMC, proopiomelanocortin; vmARH, ventromedial arcuate nucleus; VMH, ventromedial nucleus

Received July 5, 2021 • Accepted July 20, 2021 • Available online 26 July 2021

https://doi.org/10.1016/j.molmet.2021.101311

makes them susceptible to significant variations in glucose concentration, here, we investigate the different roles of tanycyte GCK in mice. The neuroanatomical analysis of GCK expression along the third ventricle revealed that this enzyme is mainly present in tanycytes facing the ventromedial ARH (vmARH) in mice. The genetic deletion of *Gck* along the third ventricle induces the ablation of this tanycyte subgroup by the activation of the BAD signaling pathway and leads to the reorganization of the ME-vmARH region. The physiological consequence of this reorganization is an intricate alteration in energy balance regulation, with opposing phenotypes, depending on the metabolic status of the animal.

2. MATERIALS AND METHODS

2.1. Mice and genotyping of transgenic animals

Two-to-four-months old male C57Bl6 mice (initially obtained from Charles River), $Gck^{cre/+}$ mice, $Gck^{f/f}$:Rosa26-floxed stop tdTomato mice [14], $Gck^{f/f}$:Rosa26-floxed stop tdTomato:Npy-GFP mice, and Rosa26-floxed stop tdTomato:Npy-GFP mice were used in this study. TaconicArtemis GmbH (Köln, Germany) generated $Gck^{cre/+}$ mice by homologous recombination in C57BL/6N embryonic stem cells. The codon-improved Cre recombinase [15] was introduced before the stop codon of *Gck* present in exon 10 and separated from the *Gck* sequence by a T2A ribosomal skipping sequence (to be described in Kessler S et al., submitted). Animals were housed in groups (from 2 to 5 mice per cage) and maintained in a temperature-controlled room (at 22−23 °C) on a 12 h' light/dark cycle with ad libitum access to diet (Diet 3436; Provimi Kliba AG, Kaiseraugst, Switzerland) and water. For genotyping, biopsies were collected and DNA extraction was performed using the HotShot method. PCR amplification was performed using KAPA2G Fast ReadyMix (KK5103, KAPA Biosystems) following the manufacturer's instructions. The primers (5′-3′) used in this study are available on request. All animal procedures were performed at the University of Lausanne and were reviewed and approved by the Veterinary Office of Canton de Vaud.

2.2. DNA recombination and tdTomato expression in tanycytes

To recombine DNA in tanycytes, TAT-CRE fusion protein (Excellgen, EG-1021) was stereotactically infused into the third ventricle (1 µl over 3 min at 2 mg/ml; diluted in saline solution (1/8)); at the coordinates from the bregma of AP = −1.7 mm; ML = 0 mm; DV = −5.3 mm (from cortex surface) of ketamine/xylazine-anesthetized mice (100 mg/kg and 20 mg/kg, respectively), as previously described [3,16]. Control mice ($TanGck^{f/f}$) were littermate mice infused with the vehicle solution (20 mM HEPES, 600 mM NaCl, 50% Glycerol, 200 mM Arginine, 1 mM DTT, pH 7.4; diluted in saline solution (1/8)). The efficiency and specificity of DNA recombination were validated by tdTomato or/and *Gck* expression.

2.3. Mouse physiology

For glucose homeostasis analysis, blood glucose measurements were made from tail vein blood using a OneTouch glucose monitor (One Touch Ultra, Bayer). We performed glucose and pyruvate tolerance tests after a 16 h fast (6 p.m.−10 a.m.) using intraperitoneal injection of 2 g of glucose or pyruvate, respectively, per kg of body weight. We performed insulin tolerance tests after a 5 h fast (9 a.m.−2 p.m.) using an intraperitoneal injection of 0.8 UI of insulin per kg of body weight. We performed 2-deoxyglucose (2-DG) tolerance test in fed mice (10 a.m.) using intraperitoneal injection of 300 mg of 2-DG per kg of body weight. Blood was collected from the tail vein 30 min after glucose injection to evaluate insulin levels measured by ELISA (#10-1247-01, Mercodia). Blood was collected from the submandibular vein 30 min after insulin injection and 1 h after 2-DG injection to evaluate glucagon levels measured by ELISA (#10-1281-01, Mercodia).

For energy balance analysis, body weight and food weight were measured using a scale. Body composition was recorded using nuclear magnetic resonance (NMR; Echo MRI). For basal food intake during the night and the day, mice were isolated, and body weight and food weight were measured at 8 a.m. and 6 p.m. every day. For short-term refeeding, mice were fasted for 24 h and then isolated 1-h before the experiment (starting at 10 a.m.). Food weight was measured at 0, 15, 30, 60, 90, 120, 180, and 240 min during refeeding. For long-term refeeding, mice were isolated two days before the experiment. After 24-h fasting, food weight was measured at 0, 2, 4, 6, and 8 h during refeeding (starting at 10 a.m.). For 2-DG induced food intake, mice were isolated 1-h before the experiment and then injected with 500 mg of 2-DG per kg of body weight (at 10 a.m.). Food weight was measured at 0, 15, 30, 60, 90, 120, and 180 min. For leptin sensitivity tests, mice were isolated 24-h before the experiment, then injected at 6 p.m. on day 1 with vehicle (intraperitoneal injection, 5 mM sodium citrate buffer, pH 4.0), and at 6 p.m. on day 2 with leptin (intraperitoneal injection, 3 mg/kg, PeproTech). Food weight was measured at 12-h and 24-h after each injection. For ghrelin sensitivity tests, mice were isolated 1-h before the experiment and then injected with 2 mg/kg ghrelin at 10 a.m.: food weight and glycemia were measured at 0, 30, and 60 min. Total energy expenditure, oxygen consumption and carbon dioxide production, food intake, and ambulatory movements were measured using calorimetric cages (Phenomaster, TSE Systems GmbH, Germany) for a week starting ten days after TAT-Cre (or vehicle) injection. Mice were individually housed and acclimatized to the cages for 48 h before experimental measurements, which consisted of monitoring mice over five consecutive days.

Body temperature was recorded using a rectal thermometer (BIO-TK8851, BIOSEB). For BAT temperature, mouse backs were shaved the day before the experiment, and the temperature was recorded using a thermal camera (FLIR E95 24°, FLIR) at 0, 30, and 60 min following 2-DG injection (500 mg/kg). Glycemia was measured at the same time points to validate 2-DG efficiency.

2.4. Tissue collection

Mice were killed between 9 a.m. and 10 a.m, at different time points after vehicle or TAT-Cre injection, in either fed, 24-h fasted, 2-h- or 4-h refed (ad libitum access to diet from 10 a.m. to 12 p.m and 10 a.m. to 2 p.m, respectively, after 24-h fasting) conditions. Different tissues were collected for further analyses.

Blood was collected by cardiac puncture using a syringe containing EDTA to measure hormonal levels in fed, 24-h fast, and 4-h refed using mouse metabolic multiplex assay (#MMHMAG-44K, Merck).

For qPCR and WB analysis on mediobasal hypothalamus, mice were anesthetized with isoflurane and sacrificed by decapitation. Mediobasal hypothalami were microdissected using a binocular microscope and put in liquid nitrogen.

For immunohistochemistry and *in situ* hybridization on fixed tissue, mice were anesthetized with isoflurane and perfused transcardially with 0.9% saline followed by an ice-cold solution of 4% paraformaldehyde in 0.1 M phosphate buffer (pH 7.4). Brains were quickly removed, postfixed in the same fixative for 2 h at 4 °C, and immersed in 20% sucrose in 0.1M phosphate-buffered saline (PBS) at 4 °C overnight. Brains were finally embedded in ice-cold OCT medium (optimal cutting temperature embedding medium, Tissue Tek, Sakura) and frozen on dry ice or in liquid nitrogen-cooled isopentane. Epididymal white adipose tissue (eWAT) and brown adipose tissue (BAT)

were also removed and postfixed in the same fixative overnight at 4 °C. Tissues were then processed for hematoxylin and eosin (H and E) staining.

For immunohistochemistry on fresh tissue, mice were anesthetized with isoflurane and sacrificed by decapitation. Brains were quickly removed, directly embedded in ice-cold OCT medium, and frozen in liquid nitrogen-cooled isopentane. Epididymal white adipose tissue (eWAT) and brown adipose tissue (BAT) were also removed and frozen in liquid nitrogen for qPCR analysis.

For pSTAT3 immunostaining, mice were injected with vehicle or leptin (intraperitoneal injection, 3 mg/kg in 5 mM sodium citrate buffer, PeproTech, France) and perfused 45 min later with a 2% paraformaldehyde in 0.1 M phosphate buffer (pH 7.4).

For electron microscopy, mice were anesthetized with isoflurane and sacrificed by decapitation. Brains were quickly removed and fixed in an ice-cold solution of 4% paraformaldehyde/5% glutaraldehyde in 0.1 M phosphate buffer (pH 7.4) for 24 h. Two hundred μm thick hypothalamic slices were then cut using vibratome and postfixed in the same fixative for 24 h. Afterward, the samples were incubated in 2% (wt/vol) osmium tetroxide and 1.5% (wt/vol) K4[Fe(CN)6] in 0.1 M PB buffer on ice for 1 h, following by 1-h incubation at ambient temperature in 1% (wt/vol) tannic acid in 0.1 M PB buffer. Subsequently, brain slices were incubated in 1% (wt/vol) uranyl acetate for 1 h and dehydrated at the end of standard gradual dehydration cycles in ethanol. Samples were flat embedded in the Epon-Araldite mix [17,18].

2.5. Molecular biology

For qPCR, RNeasy Mini kit (#74104 QIAGEN) and RNeasy Lipid Mini kit (#1023539, QIAGEN) were used to extract mRNA from frozen hypothalami and eWAT/BAT, respectively. Approximately 250 ng of RNA was then reverse-transcribed using the M-MLV reverse transcriptase (M3683, Promega) following the manufacturer's instructions. cDNAs were diluted (1:10), and qPCR was performed using GoTaq qPCR Master Mix (Promega). The primers (5′-3′) used in this study are reported in Supplementary Table 1.

For Western Blot on mediobasal hypothalami, proteins were extracted using a lysis buffer (150 M NaCl, 1% NP-40, 50 mM Tris—HCl pH 8.0, 0.5% Sodium deoxycholate, 0.1% SDS, protease inhibitor, Phosphostop), and then quantified using BCA protein assay kit (23227, Thermo Fisher). Using Laemmli loading buffer in a 12% Acrylamide/Bis Gel, 30 ug were loaded and then transferred to a nitrocellulose membrane overnight. Proteins of interest were then revealed using antibodies and the revelation was performed using the WesternBright Sirius chemiluminescent detection kit (K-12043-D20, Advansta). The antibodies used in this study are reported in Supplementary Table 1.

2.6. Immunohistochemistry and *in situ* hybridization

Brains were cut using a cryostat into 20 μm thick coronal sections (or 25 μm thick coronal sections for c-fos and pSTAT3 immunostaining, and *Wisteria floribunda* agglutinin (WFA) labeling) and processed for immunohistochemistry as described previously [5,19]. The antibodies used in this study are reported in Supplementary Table 1. For most of the antibodies, slide-mounted sections were: 1) blocked for 30 min using a solution containing 4% normal goat serum and 0.3% Triton X-100, 2) incubated overnight at 4 °C with primary antibodies (Supplementary Table 1) followed by 2 h at room temperature with a cocktail of secondary Alexa Fluor-conjugated antibodies (1:500, Molecular Probes, Invitrogen, San Diego, CA, Supplementary Table 1) and 3) counterstained with DAPI (1:10,000, Molecular Probes, Invitrogen), and 4) coverslipped using Mowiol (Calbiochem, La Jolla, CA). For pSTAT3 immunolabeling, mice were perfused with 2% PFA; slide-mounted sections were: 1) pretreated with 0.5% NaOH and 0.5% H2O2 in PSB 1x for 20 min, 2) incubated in 0.3% glycine for 10 min and then in 0.03% SDS for 10 min at room temperature, 3) blocked for 20 min at room temperature using a solution containing 1% bovine serum albumin, 4% normal goat serum and 0.4% Triton X-100, 4) incubated for 48 h at 4 °C with primary antibodies (Supplementary Table 1) in a solution containing 1% normal goat serum, 1% bovine serum albumin, and 0.4% Triton X-100 followed by 2 h at room temperature with a cocktail of secondary Alexa Fluor-conjugated antibodies, 5) counterstained with DAPI (1:10,000, Molecular Probes, Invitrogen), and 6) coverslipped using Mowiol (Calbiochem, La Jolla, CA). For perineuronal net, slices were incubated 1) in a blocking solution containing 4% normal goat serum and 0.3% Triton X-100 for 1 h at room temperature, 2) with *W. floribunda* agglutinin (WFA, 1:500, Sigma—Aldrich, Thermo Fisher) overnight at 4 °C, 3) with Streptavidin Alexa Fluor 647 conjugated secondary antibody (1:500, Thermo Fischer) for 2 h at room temperature, 4) counterstained with DAPI (1:10,000, Molecular Probes, Invitrogen), and 5) coverslipped using Mowiol (Calbiochem, La Jolla, CA).

Fixed frozen brains were cut using a cryostat into 20 μm thick coronal sections and processed for RNAscope® *in situ* hybridization following the manufacturer's instructions (ACD). Slide-mounted sections were first: 1) incubated in a boiling 1X target retrieval solution for 5 min, and 2) incubated at 40 °C with Protease III solution for 30 min. The sequential hybridizations were then performed following the manufacturer's instructions. The probes used in this study are reported in Supplementary Table 1.

2.7. Microscopic imaging

Sections were analyzed using a ZEISS Axio Imager. M2 microscope, equipped with ApoTome.2 and a Camera Axiocam 702 mono (Zeiss, Germany). Specific filter cubes were used for the visualization of green (Filter set 38 HE eGFP shift-free (E) EX BP 470/40, BS FT 495, EM BP 525/50), red (Filter set 43 HE Cy 3 shift-free (E) EX BP 550/25, BS FT 570, EM BP 605/70), far-red (Filter set 50 Cy 5 shift-free (E) EX BP 640/30, BS FT 660, EM BP 690/50), and blue (Filter set 49 DAPI shift-free (E) EX G 365, BS FT 395, EM BP 445/50) fluorescence. Different magnifications were selected using a Zeiss x20 objective (Objective Plan-Apochromat 20x/0.8 M27 (FWD = 0.55 mm)) and a 63 × oil-immersion objective (Objective C Plan-Apochromat 63x/1.4 Oil DIC M27 (FWD = 0.14 mm)). To create photomontages, images were acquired using ZEN 2.3 pro software using Z-Stack and Tiles/Positions ZEN modules for each fluorophore, sequentially. Quintuple-ApoTome frames were collected stepwise over a defined z-focus range corresponding to all visible fluorescence within the section: multiple-plane frames were collected at a step of 1 μm while using x20 objective (between 4 and 10 frames per image). All images were then saved in. cvi, processed to get orthogonal and maximal intensity projections, and finally exported in. tiff. For the processing steps (i.e., adjust brightness and contrast, change colors, and merge images using Adobe Photoshop (Adobe Systems, San Jose, CA)).

2.8. Electron microscopy

Flat embedded samples were mapped using binocular to map the precise region of interest at the basal part of the ventricle. For the ultramicrotome sectioning, samples were carefully oriented inside the holder according to the correlation maps derived from the embedded samples. Polymerized flat blocks were trimmed using a 90° diamond trim tool. The arrays sequential sections of 100 nm were generated using a 35° ATC diamond knife (Diatome, Biel, Switzerland) mounted on Leica UC6 microtome (Leica, Vienna). Arrays that covered the span

of the ROI were transferred on pieces of silicon wafer [20]. Wafers were analyzed using an FEI Helios Nanolab 650 scanning electron microscope (Thermo Fischer, Eindhoven). Wafers were screened to target the relevant sections, and the ventricle area was imaged by tiling multiple images using the following imaging settings: MD detector, accelerating voltage 2 kV, current 0.8 nA, and dwell time 4–6 µs. Subsequently, relevant areas were re-imaged using higher resolution parameters, collected either manually or using the AT module of MAPs program (Thermo Fischer, Eindhoven) [20]. For electron microscopy data interpretation, previous reports in the literature were used to recognize the different neural cell types based on their ultrastructural characteristics [5,21].

2.9. Analysis

Gene expression levels from public available single hypothalamic cells in the hypothalamus [22] were downloaded from NCBI (accession number # GSE93374) and processed for downstream analysis using Seurat [23].

For brain image analyses, the entire ARH was divided into four subregions on the anteroposterior axis, corresponding to zone 1 (from bregma −1.3 to −1.6 mm), zone 2 (from bregma −1.6 to −1.8 mm), zone 3 (from bregma −1.8 to −2.1 mm), and zone 4 (from bregma −2.1 to −2.5 mm). These subregions have been fully characterized previously [5].

For *Gck* expression analysis, one section per anteroposterior zone was used for quantification. The low *Gck* expression along the ventricle allowed us to perform this quantification by counting the number of *Gck* mRNAs detected by RNAscope in the ventricular layer. The ventricular layer facing the median eminence or the vmARH (in µm2) was delineated by DAPI staining. For cell nuclei and neuronal density, two sections per anteroposterior zone were used for quantification. The number of DAPI-positive nuclei and HuC/D-positive cells was quantified in the ARH, the VMH, and the DMH. The quantification was restricted to a 20,000 μm^2 square area close to the ventricular layer.

For NPY neuron analysis, two sections per anteroposterior zone were used for quantification. The total number of NPY neurons and the number of NPY neurons surrounded by WFA-labelled perineuronal net were quantified. NPY neuron diameter was measured using Imaris® software.

For CRH and TRH neurosecretion analysis, two sections per anteroposterior zone were used for quantification. Pictures were acquired using the same parameters and densitometric analysis was performed using ImageJ software.

For fenestrated vessel analysis, the number of MECA32-positive vessels was quantified on the entire anteroposterior axis as previously reported [3]. For ZO1 immunostaining along the ventricle and BBB vessels, two sections per anteroposterior zone were used for quantification. Densitometric analysis was performed using ImageJ software as previously described [3].

For pSTAT3 and c-Fos analysis, two sections per anteroposterior zone were used for quantification. The ARH was delimited using DAPI counterstaining and the number of pSTAT3-or c-Fos-positive cells was quantified using ImageJ software.

For eWAT analysis, images were processed using the Adiposoft plugin on ImageJ software. Two sections per animal were used for quantification. For BAT analysis, images were binarized and skeletonized using ImageJ software, and the integrated density was then calculated. Two sections per animal were used for quantification.

For metabolic cages, analyses were performed following standard procedures [24].

For qPCR analysis, gene expression levels were normalized to TATA-binding protein (TBP) using the $2-\Delta\Delta Ct$ method and were presented as relative transcript levels. For western blot, densitometric analysis was performed using ImageJ software.

2.10. Statistical analysis

All values are expressed as means ± SEM. Data were analyzed for statistical significance with Graph Prism 5 software (Version 11.0), using unpaired t-test, one-way ANOVA followed by a Tukey's post hoc test, or two-way ANOVA followed by a Bonferroni's post hoc test when appropriate. P-values of less than 0.05 were considered to be statistically significant.

3. RESULTS

3.1. Glucokinase is expressed in vmARH tanycytes facing NPY neurons

To analyze GCK expression in mouse tanycytes, we combined single-cell RNAseq, *in situ* hybridization, gene reporter assay, and immunohistochemistry. We first investigated a published single-cell RNAseq dataset from 20,921 cells dissociated from mediobasal hypothalami [22]. Approximately 2085 *Gck*-expressing cells were subsetted and clustered into distinct cell types (Supplementary Figure 1A). Neurons represented the main *Gck*-expressing cell population within the hypothalamus (Supplementary Figure 1A–B). However, a small cluster expressing known tanycyte markers was also present (Supplementary Figure 1A–B). Unfortunately, the small number of these cells and their different metabolic states (i.e., chow, fed, and high-fat diet) (Supplementary Figure 1C) did not allow us to analyze this cluster further.

In situ hybridization was then performed using RNAscope to visualize *Gck*-expressing tanycytes (Figure 1A–C). *Gck* mRNAs were successfully detected in the mediobasal hypothalamus (Figure 1A–C). They were expressed at a high level in the ARH parenchyma (Figure 1A). Along the third ventricle, *Gck* mRNAs were mainly located in tanycytes lining the corner of the infundibular recess and facing the vmARH (Figure 1B–C), corresponding to ventral and dorsal β1 tanycytes in the Akmayev classification [25]. As previously reported in rats [26], refeeding increases *Gck* mRNA expression in ME and vmARH tanycytes (Supplementary Figure 1D–G). To identify *Gck*-expressing tanycytes using an alternative approach, $Gck^{cre/+}$ mice were injected with AAV-DIO-mCherry in the lateral ventricle, and the cells expressing mCherry were identified two weeks later by fluorescence microscopy. mCherry was found to be present in elongated cells lining the corner of the infundibular recess (Figure 1D–E), overlapping *in situ* hybridization data (Figure 1A–C). These cells had a typical tanycyte shape (Figure 1D–E). mCherry was also present in some parenchymal cells located in the ARH (Figure 1D–E). To finally validate the presence of GCK protein in tanycytes, immunohistochemistry was performed on mouse hypothalamic brain sections (Figure 1F–H). As previously described in rats [26,27], the GCK protein was present along the third ventricle in tanycytes facing the vmARH, as it colocalized with the tanycyte marker vimentin (VIM) (Figure 1G–H). By combining these *in situ* hybridization and immunohistochemistry data, we further established a *Gck* expression map on the anteroposterior axis. *Gck* was expressed in tanycytes from Bregma −1.5 to −2.2 (Figure 1I), highlighting issues in the Akmayev classification. However, GCK was expressed at the very bottom of the third ventricle in the anterior part, whereas it was restrained to the vmARH, caudally (Figure 1I). At the site of pituitary stalk formation, *Gck* was no longer observed along the third ventricle (Figure 1I).

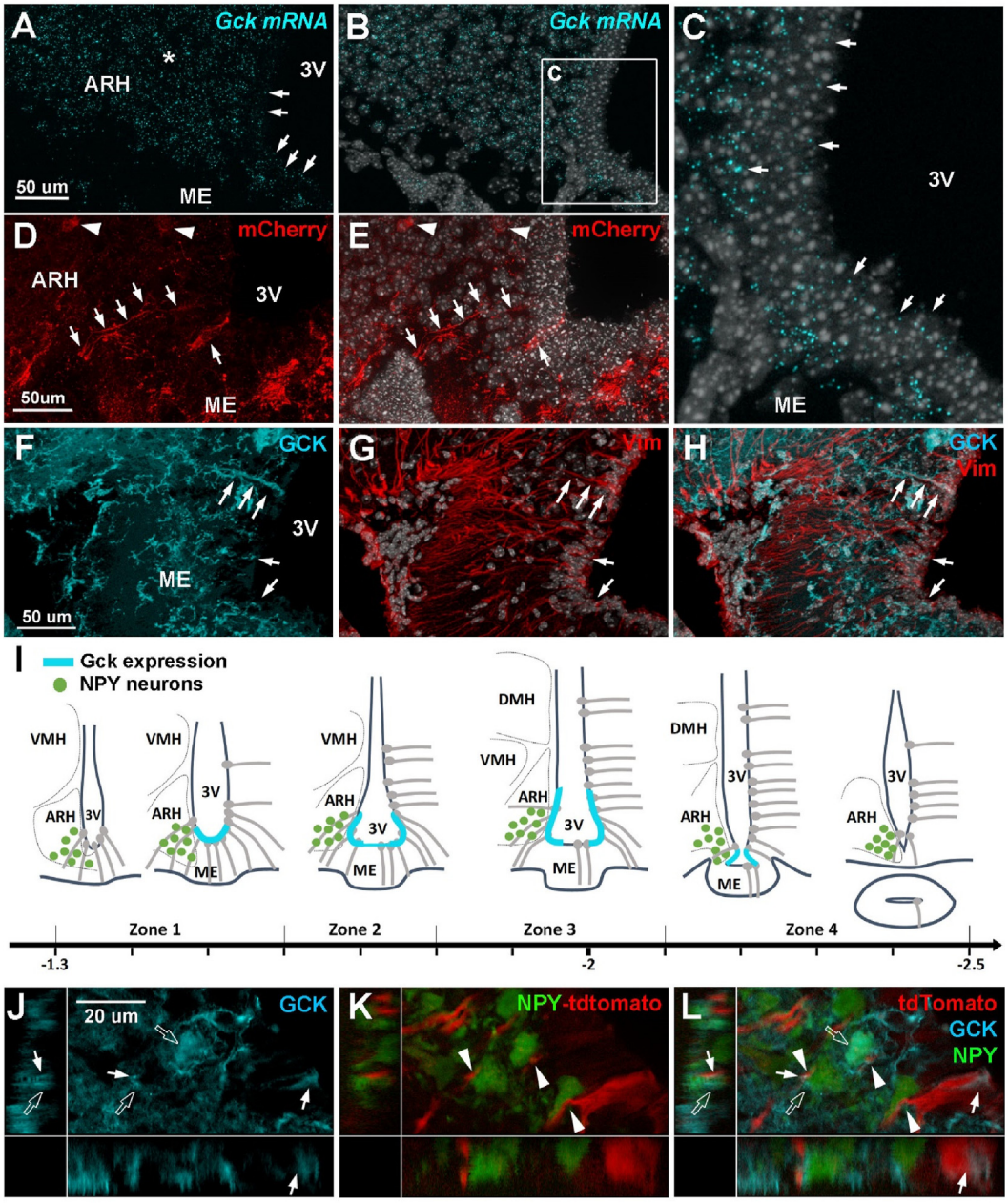

Figure 1: Glucokinase is expressed in tanycytes facing the ventromedial arcuate nucleus. **A-C.** Representative images of *Gck* mRNA expression (cyan dots) along the third ventricle (arrows in A and C) and in the ARH parenchyma (asterisk in A) in adult male mice. **D-E.** Representative images of *Gck* promoter activity (mCherry, red) along the third ventricle (arrows) and in parenchymal cells (arrowheads) in adult male mice. **F—H.** Representative images of GCK immunostaining (cyan) along the ventricle (arrows). GCK staining colocalizes with vimentin staining (red in G and H). **I.** Schematic representation of *Gck* expression (cyan) along the third ventricle on the anteroposterior axis, based on *in situ* hybridization and immunohistochemistry analysis. **J-L.** Representative images of tanycyte (tdTomato, red)/NPY neuron (green) units in the vmARH. Tanycytes contact NPY neurons (arrowheads in K and L). GCK (cyan) is expressed in tanycytes (arrows) and NPY neurons (empty arrows). ARH, arcuate nucleus; DMH, dorsomedial nucleus; GCK, glucokinase; ME, median eminence; NPY, neuropeptide Y; Vim, vimentin; vmARH, ventromedial arcuate nucleus; VMH, ventromedial nucleus; 3V, third ventricle. Cell nuclei are counterstained using DAPI (white in B, C, E, G, H). Scale bars: 50 μm in A, D, F, and 20 μm in J. Refer Supplementary Figure 1.

Finally, we analyzed the association between *Gck*-expressing tanycytes and NPY neurons, key tanycyte partners within the vmARH [5]. As previously reported [5,28], tanycytes contact NPY neurons through peculiar protrusions along their basal process. Interestingly, GCK-positive tanycytes contact both GCK-positive NPY neurons and GCK-negative NPY neurons (Figure 1J-L), suggesting that heterogeneous tanycyte/NPY neuron partnerships exist.

3.2. Glucokinase deletion in tanycytes induces tanycyte death and a morphological reorganization of the ME-ARH region

To study the role of GCK in tanycytes, we next deleted *Gck* in the ependymal layer in adult male mice. For this, TAT-Cre recombinase was injected into the third ventricle of tdTomatoSTOP:*Gck* floxed mice. TAT-Cre is a recombinant cell-permeant fusion Cre-recombinase protein that allows for rapid and specific DNA recombination at loxP sites, as

reported previously [3,5,16]. As TAT-Cre does not cross the ventricle wall [16], the recombination occurs in the ependyma, particularly in tanycytes (Figure 2A—B). Moreover, TAT-Cre integrates cells close to the injection site [16]. Its controlled injection within the third ventricle allowed us to mainly target the third ventricle without targeting choroid plexuses and ependymal cells located in the lateral and fourth ventricles (Supplementary Figure 1H—J). However, it is worth noting that pars tuberalis (Figure 2B) and few astrocytes and neurons present along the cannula trajectory or in contact with the cerebrospinal fluid (Supplementary Figure 1K-N) may be targeted. Using tdTomato as a

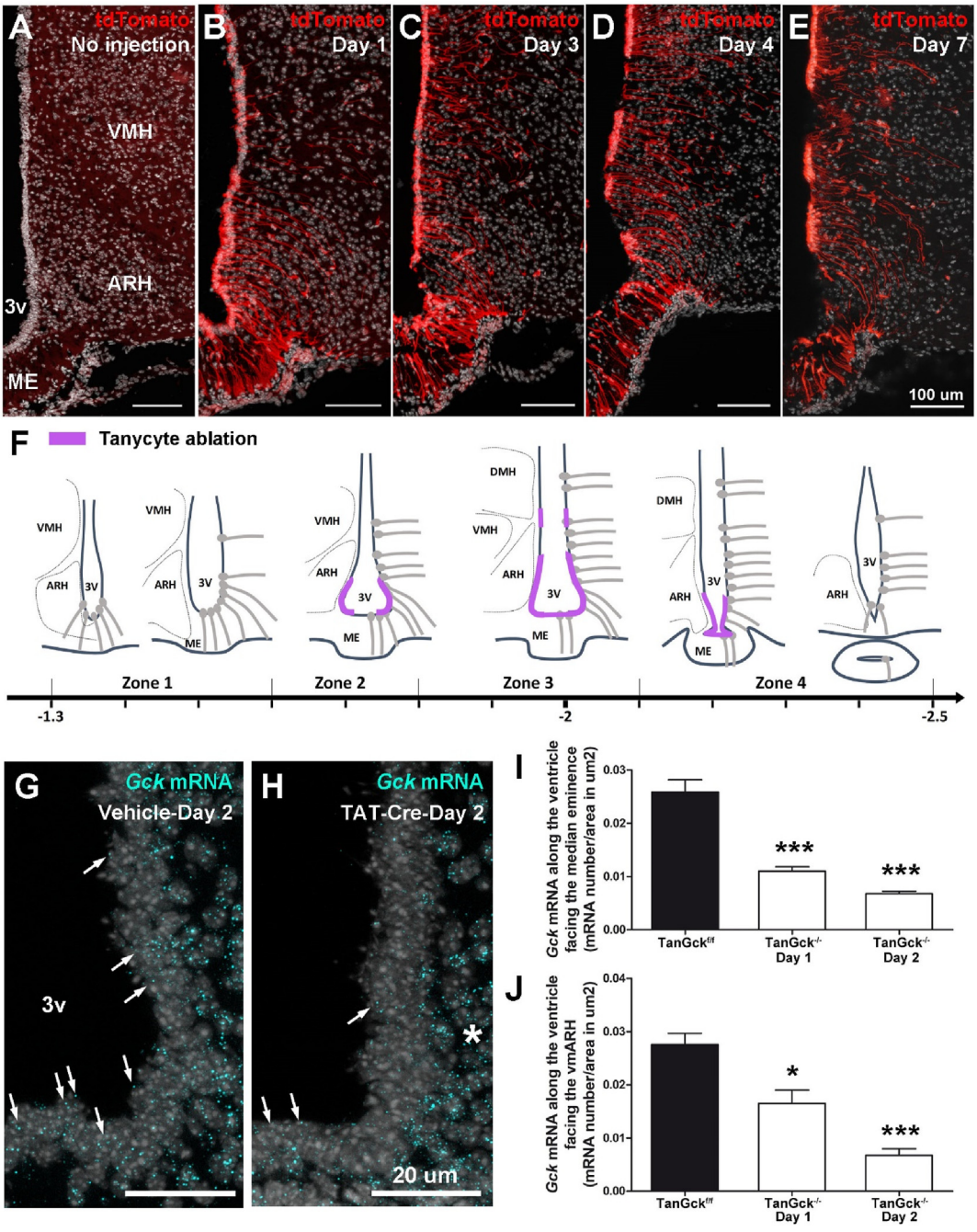

Figure 2: Glucokinase deletion in ependymal cells induces the ablation of tanycytes facing the median eminence, the ventromedial arcuate nucleus, and the ventromedial nucleus. **A-E.** Representative images of tdTomato expression along the third ventricle one, three, four, and seven days following TAT-Cre injection in TanGck$^{f/f}$ mice. Tanycytes facing the vmARH and the VMH disappear at days 3 and 4, respectively. **F.** Schematic representation of tanycyte ablation along the third ventricle on the anteroposterior axis in TanGck$^{-/-}$ mice. **G-H.** Representative images of *Gck* mRNA expression (cyan dots) along the third ventricle (arrows) in TanGck$^{f/f}$ and TanGck$^{-/-}$ mice two days after the injection. *Gck* mRNA is reduced along the ventricle, whereas it is still present in the brain parenchyma in TanGck$^{-/-}$ mice (asterisk). **I-J.** Quantification of *Gck* expression in tanycytes facing the ME (I) and the vmARH (J) in TanGck$^{f/f}$ and TanGck$^{-/-}$ mice one and two days after the injection (n = 6 TanGck$^{f/f}$; n = 4/3 TanGck$^{-/-}$ mice at day 1 and day 2, respectively). ARH, arcuate nucleus; DMH, dorsomedial nucleus; GCK, glucokinase; ME, median eminence; VMH, ventromedial nucleus; 3V, third ventricle. Cell nuclei are counterstained using DAPI (white in A-E, G-H). Scale bars: 100 μm in A-E and 20 μm in G-H. Data are means ± SEM. *p < 0.05; ***p < 0.001 compared to TanGck$^{f/f}$ group. Refer Supplementary Figure 1—5.

reporter, DNA recombination was observed along the third ventricle the next day after TAT-Cre injection (Figure 2A—B). Between two and three days after TAT-Cre injection, tanycytes facing the vmARH disappeared in TanGck$^{-/-}$ mice (Figure 2C—D). On the anteroposterior axis, tanycyte ablation was detected from Bregma −1.6 to −2.2 and corresponded to the tanycyte subgroup expressing *Gck* (Figure 2F). One week after TAT-Cre injection, vmARH tanycytes and a small tanycyte subgroup facing the VMH (Figure 2E—F) had disappeared. To genetically characterize the tanycyte subpopulation impacted by *Gck* deletion, qPCR analysis was performed on microdissected hypothalami to measure the expression of tanycyte markers: *Fgf10* mRNA decreased, whereas *Vim* mRNA was unchanged (Supplementary Figure 1O), suggesting that the β tanycyte population was reduced. Global *Gck* expression was stable in the mediobasal hypothalamus (Supplementary Figure 1O), suggesting that TAT-Cre injection did not induce *Gck* deletion in parenchymal cells or a genetic compensation in the region.

Although TAT-Cre is commonly used in various studies without inducing tanycyte death [3,5], we performed control experiments to confirm that tanycyte disappearance was because of *Gck* deletion (Supplementary Figure 1P—R). First, TAT-Cre was stereotactically injected in C57Bl6 and tdTomato mice: no cell death was observed one week after the injection (Supplementary Figure 1P—Q). Additionally, adenoviruses expressing Cre-recombinase were used to delete *Gck* in tanycytes, which resulted in similar tanycyte ablation (Supplementary Figure 1R). To finally validate the deletion of *Gck* mRNA, specifically in tanycytes, *in situ* hybridization was performed for two days after TAT-Cre injection. *Gck* mRNA expression decreased in tanycytes facing the lateral ME and the vmARH in TanGck$^{-/-}$ mice (Figure 2G—J).

As cell ablation may profoundly alter the region, a detailed investigation of hypothalamic morphology was carried out (Supplementary Figure 2—4). Hypothalamic cell and neuronal density in the ARH, the VMH, and the DMH were similar in TanGck$^{-/-}$ compared to TanGck$^{f/f}$ mice (Supplementary Figure 2A—D). Similar results were obtained on the anteroposterior axis (Supplementary Figure 4A—B). With regard to the impact of tanycyte ablation on arcuate neurons, the number and diameter of NPY neurons were constant in TanGck$^{-/-}$ compared to TanGck$^{f/f}$ mice (Supplementary Figure 2E-G and 4C-D). However, the number of NPY neurons surrounded by a perineuronal net decreased in zone 3 (Supplementary Figure 4E), while no differences were globally observed (Supplementary Figure 2H—J). No differences were observed in the neurosecretion of CRH and TRH; the two neurohormones involved in the regulation of energy balance (Supplementary Figure 2K-P). Finally, the expression of arcuate neuropeptides involved in the regulation of energy balance, such as *Npy*, *Cart*, *Agrp, and Pomc* mRNA was unaffected in basal conditions (Supplementary Table 2).

Regarding the organization of the blood/brain interface, some tdTomato-positive (Figure 2F) or vimentin-positive (Supplementary Figure 3A—H) processes were still visible in the brain parenchyma in TanGck$^{-/-}$ mice, while tanycyte cell bodies were absent along the ventricle. Instead, a GFAP-positive glial scar was present (Supplementary Figure 3A—H). Additionally, the tanycyte barrier carried by β tanycytes and its plasticity observed during energy imbalance [3] were profoundly altered in TanGck$^{-/-}$ mice (Supplementary Figure 3I-O and 5). In TanGck$^{f/f}$, MECA-32-positive fenestrated vessels faced tanycytes expressing ZO1 tight junction proteins organized in continuous belts around their cell bodies. These tight junction complexes and deep interdigitations were also observed between tanycyte apical poles using electron microscopy (Supplementary Figure 5). During fasting, the number of MECA-32-positive fenestrated loops increased in the vmARH (Supplementary Figure 3K-N) and correlated with the reorganization of ZO1 tight junction proteins (Supplementary Figure 3O). In TanGck$^{-/-}$ mice, ZO1 immunostaining was absent along the ventricle, and the number of fenestrated loops did not increase in the ME and the vmARH in fasting conditions (Supplementary Figure 3I-N). This alteration mainly occurred in zones 2 and 3 (Supplementary Figure 4G). Blood—brain barrier vessels located in the ARH and VMH did not present significant changes in ZO1 intensity (Supplementary Figure 3P—R and 4H).

3.3. Glucokinase ensures tanycyte survival by preventing the apoptotic BAD signaling pathway

In the view of cell morphology (Figure 2F) and the literature [29], we hypothesized that tanycyte ablation was mainly caused by apoptosis (Figure 3). As GCK binds proapoptotic molecule BAD and prevents apoptosis in β-cells [13,30,31], we tested the role of the BAD signaling pathway in tanycyte death (Figure 3A—C). Two days after *Gck* deletion, BAD protein levels were unchanged in TanGck$^{-/-}$ mice, whereas its phosphorylation was lower (Figure 3A—C), suggesting that BAD activation was mainly post-translational. Caspase 3 protein levels were also raised in TanGck$^{-/-}$ mice (Figure 3D—E), while *Casp3* mRNA did not change (Figure 3H). Moreover, the expression of genes coding for proteins involved in the BAD signaling pathway increased in TanGck$^{-/-}$ mice, in particular, anti-apoptotic *Bcl2* and *Bcl-xl* (Figure 3H), suggesting a compensatory mechanism. Finally, while AMPK activation has been associated with apoptosis in the absence of GCK [32], no change in AMPK expression or/and phosphorylation was observed in the mediobasal hypothalamus (Figure 3F—H), suggesting that tanycyte disappearance was unrelated to AMPK activation.

To validate that apoptosis occurs in tanycytes, we performed immunohistochemistry against cleaved caspase-3 for two days after TAT-Cre injection. Activated caspase-3 was visible in vmARH and ME tanycytes, mainly in tdTomato-positive cells and in few tdTomato-negative cells (Figure 3I-L). Few tanycytes were already absent along the vmARH (Figure 3J). To further analyze this point, we performed electron microscopy to visualize the vmARH ependyma between the second and the third day, postinjection (i.e., when vmARH tanycytes were dying) (Supplementary Figure 5). In TanGck$^{f/f}$ mice, interdigitations and tight junctions characterized the tanycyte ependyma (Supplementary Figure 5). In TanGck$^{-/-}$ mice, the ependyma was mostly destroyed, leading to the disappearance of tanycyte-to-tanycyte connections (Supplementary Figure 5). Few remaining tanycytes displayed chromatin condensation in their nucleus, a marker of apoptosis (Supplementary Figure 5).

3.4. Ablation of glucokinase-expressing tanycytes increases adiposity

To evaluate the impact of tanycyte ablation on the regulation of metabolic physiology, we next phenotyped the mice from one to eight weeks after *Gck* deletion. Bodyweight remained comparable in both groups during the first weeks after ablation, but progressively increased in TanGck$^{-/-}$ mice till it became significantly different at week 8 (Figure 4A). In contrast, delta values for bodyweight calculated for each mouse were significantly higher in TanGck$^{-/-}$ mice immediately two weeks after *Gck* deletion (Figure 4B). This increase in bodyweight was associated with an increase in adiposity and a decrease in lean mass revealed four weeks after the injection (Figure 4C—E, Supplementary Table 2). Glycemia was mostly stable between groups in basal conditions or during energy imbalance (Supplementary Table 2). However, it is worth noting that glycemia was higher in TanGck$^{-/-}$ mice in the

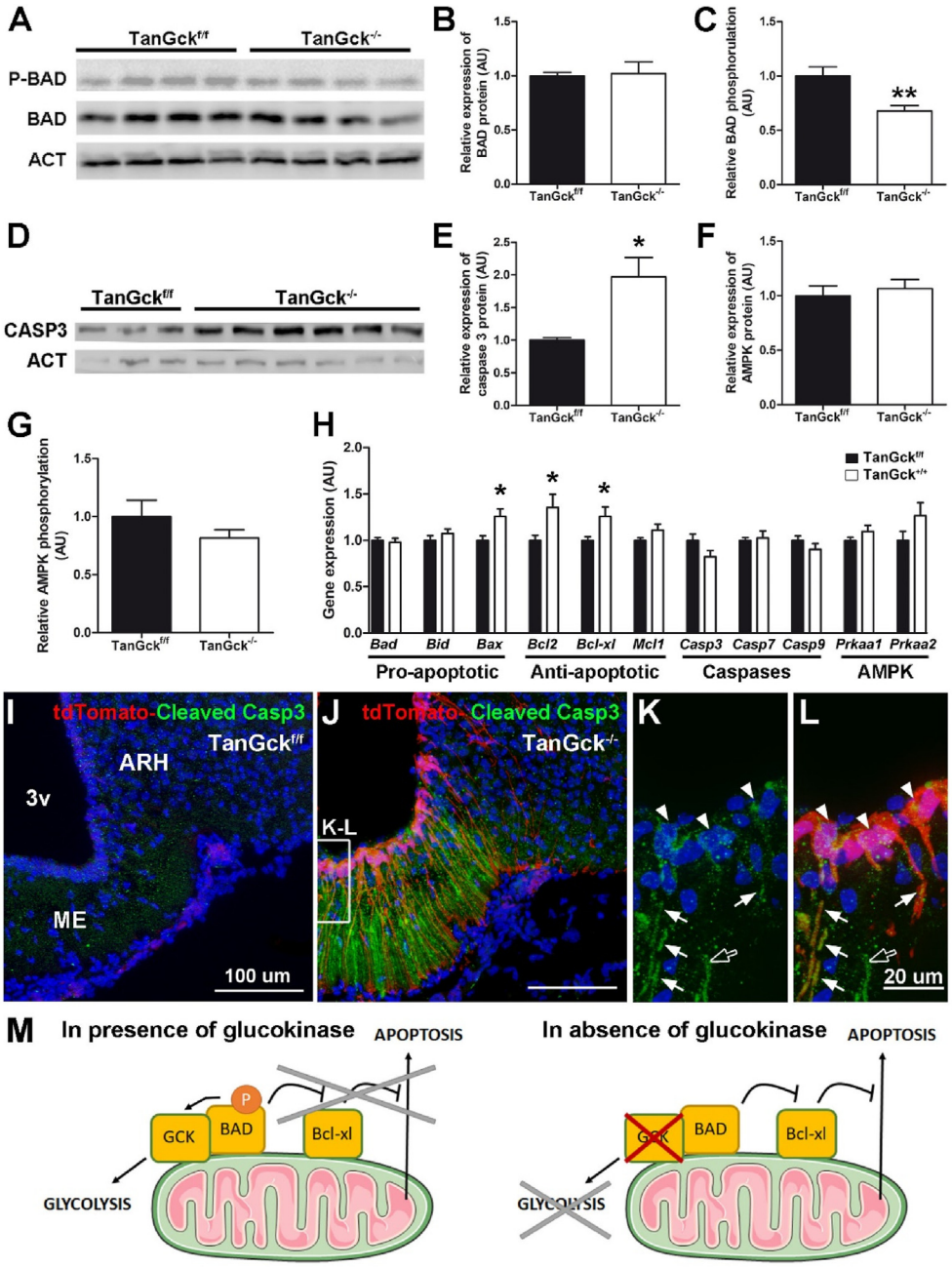

Figure 3: Glucokinase deletion induces tanycyte death through the BAD signaling pathway. **A.** Immunoblot showing phosphor-BAD, BAD, and actin (ACT) protein levels in microdissected hypothalami from TanGck$^{f/f}$ and TanGck$^{-/-}$ mice two days after the injection. **B–C.** Immunoblot analysis of BAD protein levels and BAD phosphorylation in TanGck$^{f/f}$ and TanGck$^{-/-}$ mice two days after the injection (n = 7/10, respectively). **D.** Immunoblot showing caspase-3 (CASP3) and actin (ACT) protein levels in microdissected hypothalami from TanGck$^{f/f}$ and TanGck$^{-/-}$ mice two days after the injection. **E.** Immunoblot analysis of Caspase-3 levels in TanGck$^{f/f}$ and TanGck$^{-/-}$ mice two days after the injection (n = 7/10, respectively). **F-G.** Immunoblot analysis of AMPK protein levels and AMPK phosphorylation in TanGck$^{f/f}$ and TanGck$^{-/-}$ mice two days after the injection (n = 6/10, respectively). **H.** Gene expression analysis in microdissected hypothalami from TanGck$^{f/f}$ and TanGck$^{-/-}$ mice two days after the injection (n = 11/13 per group for proapoptotic, antiapoptotic, and caspase gene; n = 5/7 per group for AMPK gene). **I-L.** Representative images of cleaved caspase-3 expression along the third ventricle in TanGck$^{f/f}$ and TanGck$^{-/-}$ mice two days after the injection. Cleaved caspase-3 is present in tdTomato-positive tanycytes (in cell bodies (arrowheads) and processes (arrows) in K-L) and tdTomato-negative tanycyte processes (empty arrow in K-L). **M.** Schematic diagram summarizing the underlying mechanisms of tanycyte death following *Gck* deletion. ACT, actin; ARH, arcuate nucleus; BAD, Bcl-2-associated death promoter; Bcl-xl, B-cell lymphoma-extra large; CASP3, caspase 3; GCK, glucokinase; ME, median eminence; 3v, third ventricle. Cell nuclei are counterstained using DAPI (blue in I-L). Scale bars: 100 μm in I-J and 20 μm in L. Data are means ± SEM. *p < 0.05; **p < 0.01 compared to TanGck$^{f/f}$ group. Refer Supplementary Figure 5.

morning four weeks after *Gck* deletion. Insulin, glucagon, ghrelin, and peptide YY (PYY) levels were comparable between groups, whereas serum leptin levels increased in TanGck$^{-/-}$ mice (Supplementary Table 2), consistent with the increased adiposity.

To further study the increase in adiposity and its consequences, epididymal white adipose tissue (eWAT) and brown adipose tissue (BAT) were analyzed by histology (Figure 4F-L) and qPCR (Figure 4M–N). Histologically, eWAT did not display significant changes with regard to

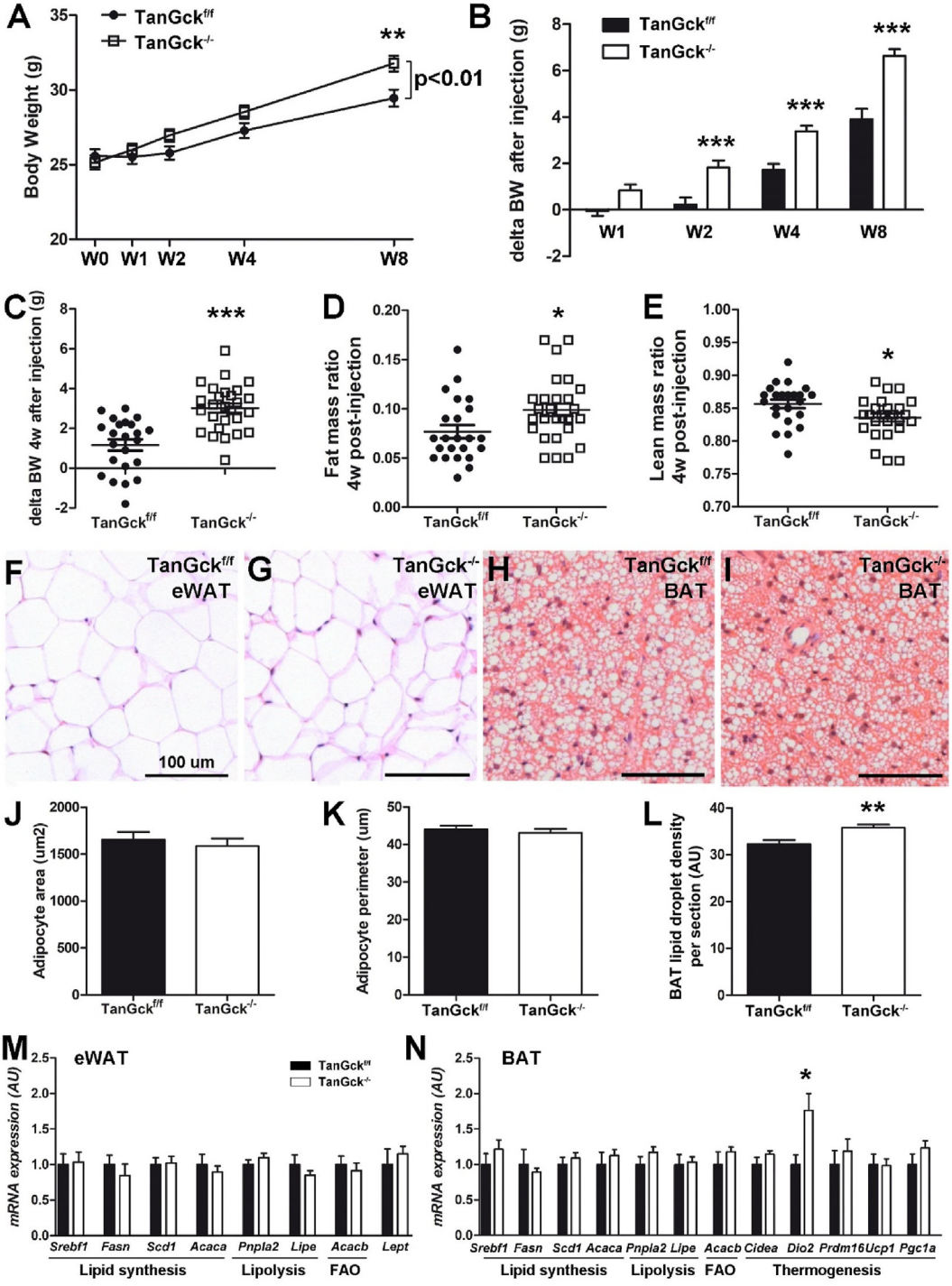

Figure 4: Tanycyte ablation increases adiposity. **A-B.** Bodyweight (A) and changes in bodyweight (compared to preinjection bodyweight) (B) in adult male TanGck$^{f/f}$ and TanGck$^{-/-}$ mice (2 cohorts, n = 16/19, respectively). **C-E**. Changes in bodyweight (C), fat mass ratio (D), and lean mass ratio (E) in adult male TanGck$^{f/f}$ and TanGck$^{-/-}$ mice four weeks after the injection (3 cohorts, n = 23/27, respectively). **F—I.** Representative images of epididymal white adipose tissue (eWAT, F-G) and subscapular brown adipose tissue (BAT, H—I) in adult male TanGck$^{f/f}$ (F, H) and TanGck$^{-/-}$ (G, I) mice. **J-K.** Quantification of mean area (J) and mean perimeter (K) of eWAT adipocytes in adult male TanGck$^{f/f}$ and TanGck$^{-/-}$ mice (n = 3/3). **L.** Quantification of BAT lipid droplet density in adult male TanGck$^{f/f}$ and TanGck$^{-/-}$ mice (n = 6/6). **M-N.** Gene expression in eWAT (M) and BAT (N) in a refed state in adult male TanGck$^{f/f}$ and TanGck$^{-/-}$ mice (n = 6/10, respectively). BAT, brown adipose tissue; eWAT, epididymal white adipose tissue; FAO, fatty acid oxidation; GCK, glucokinase; W (in A-B), week. Scale bars: 100 μm in F—I. Data are means ± SEM. *p < 0.05; **p < 0.01; ***p < 0.001 compared to TanGck$^{f/f}$ group. Refer Supplementary Table 2.

the area and perimeter of adipocytes (Figure 4F—G, J-K), suggesting that the increase in adiposity was caused by an increase in the number of adipocytes or related to other white adipose tissue pads. In contrast, BAT was leaner in TanGck$^{-/-}$ mice (Figure 4H—I, L). No change in gene expression was observed in eWAT (Figure 4M). In particular, *Lept* expression was unchanged between groups (Figure 4M), suggesting that the increase in serum leptin levels relied on an increase in fat mass rather than an increase in gene expression in eWAT. Regarding BAT,

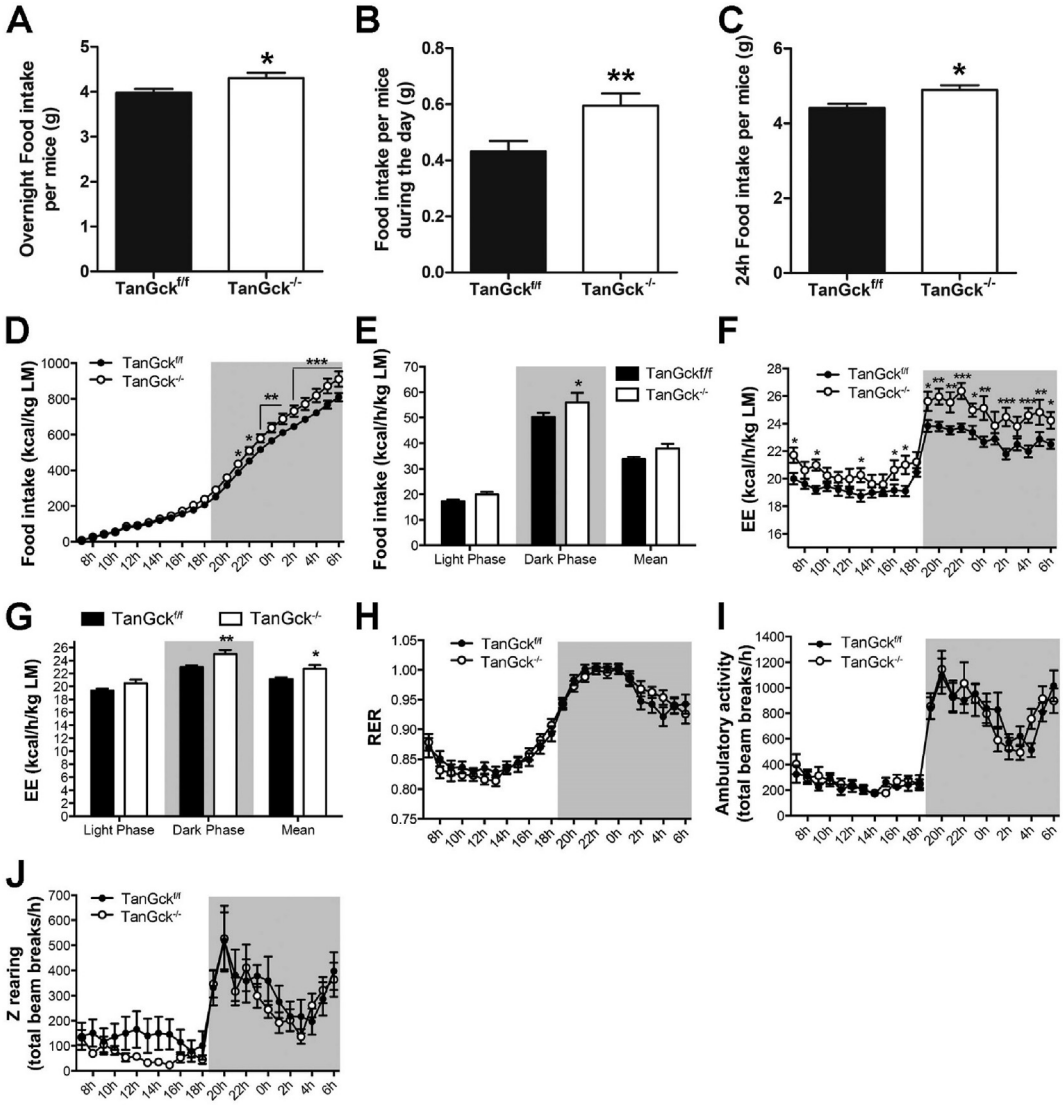

Figure 5: Tanycyte ablation increases food intake and energy expenditure. **A-C.** Nocturnal (A), diurnal (B), and 24-h (C) food intake in adult male TanGck$^{f/f}$ and TanGck$^{-/-}$ mice (4 cohorts, n = 29/35, respectively). **D-J.** Food intake (D—E), energy expenditure (F—G), RER (H), ambulatory activity (I), and Z rearing (J) in adult male TanGck$^{f/f}$ and TanGck$^{-/-}$ mice two weeks after the injection (2 cohorts, n = 12/12). Data are means ± SEM. *p < 0.05; **p < 0.01; ***p < 0.001 compared to TanGck$^{f/f}$ group. Refer Supplementary Figure 6 and Supplementary Table 2.

Dio2 gene expression increased in TanGck$^{-/-}$ mice (Figure 4N), suggesting an increase in thermogenesis.

3.5. Ablation of glucokinase-expressing tanycytes impacts energy balance and response to hypoglycemia

To determine the cause of increased adiposity, we first analyzed food intake. TanGck$^{-/-}$ mice ate more than TanGck$^{f/f}$ mice during the night and the day (Figure 5A—C). The hyperphagic phenotype appeared ten days after *Gck* deletion (Supplementary Table 2).

As energy balance also relies on energy expenditure, TanGck$^{f/f}$ *versus* TanGck$^{-/-}$ mice were then phenotyped for total energy expenditure, oxygen consumption, carbon dioxide production, and ambulatory movements using calorimetric cages for a week, starting ten days after the injection (Figure 5D—J). This time point corresponds with the beginning of the hyperphagic phenotype without changes in body composition. As reported with our manual recording, food intake increased in TanGck$^{-/-}$ mice during the dark phase (Figure 5D—E). Interestingly, energy expenditure also increased in TanGck$^{-/-}$ mice, especially during the dark phase (Figure 5F—G), whereas RER, ambulatory activity, and z-rearing did not change (Figure 5H—J). While the increase in energy expenditure did not rely on an increase in locomotor activity (Figure 5I) or on fatty acid oxidation in eWAT (Figure 4M), it may be attributed to an alteration in thermoregulation, as suggested by BAT histology (Figure 4H—I, L) and gene expression (Figure 4N). However, no difference in rectal temperature was observed in basal conditions (Supplementary Table 2) or during energy imbalance (Supplementary Figure 6A).

Regarding glucose homeostasis, glucose, pyruvate, and insulin tolerance were similar in TanGck$^{-/-}$ mice compared to TanGck$^{f/f}$ mice (Supplementary Figure 6B—E). As increased adiposity may induce insulin intolerance over the long term, similar experiments were performed twelve weeks after *Gck* deletion: Once again, no difference was observed between TanGck$^{f/f}$ and TanGck$^{-/-}$ groups (data not shown). However, insulin injection induced lower glucagon secretion in

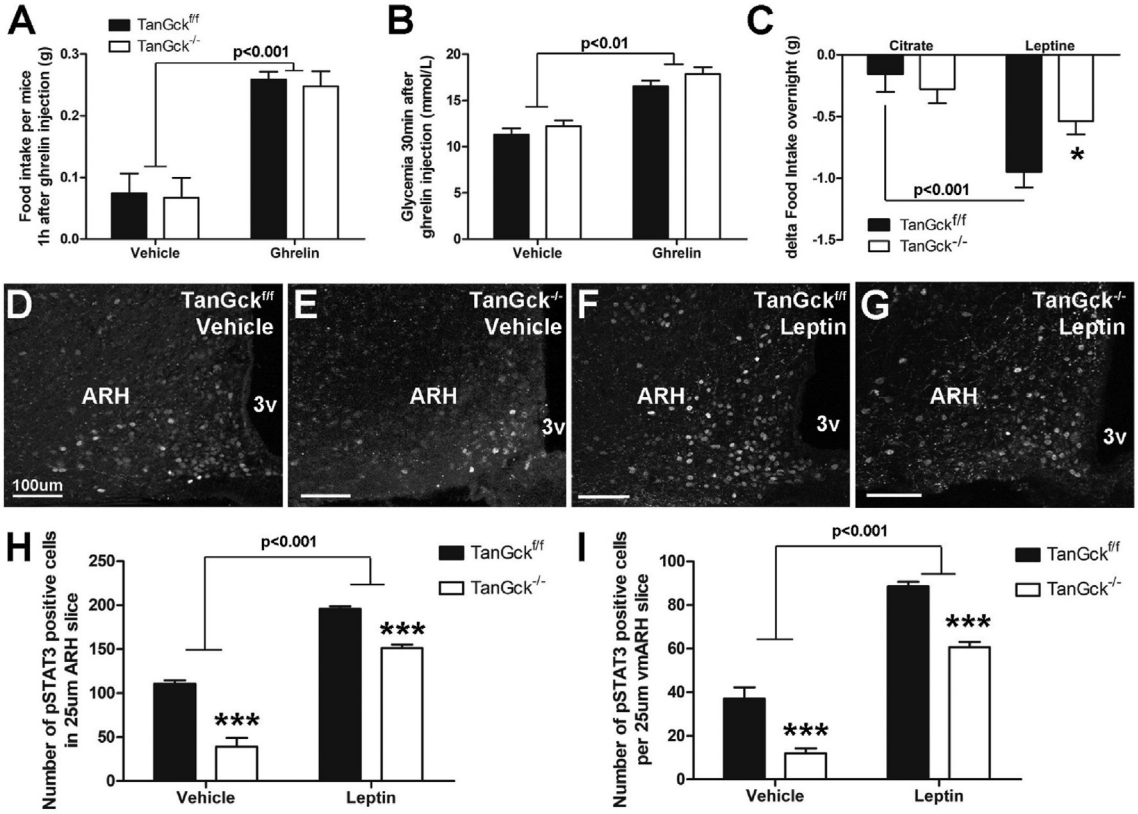

Figure 6: Tanycyte ablation induces leptin resistance. **A-B.** 1-h food intake (A) and 30-min glycemia (B) after ghrelin injection in adult male TanGck$^{f/f}$ and TanGck$^{-/-}$ mice (2 cohorts, n = 6/5 in vehicle condition; n = 5/11 in ghrelin condition, respectively). **C.** Difference in overnight food intake in adult male TanGck$^{f/f}$ and TanGck$^{-/-}$ mice following citrate or leptin injection (2 cohorts, n = 13/15, respectively). **D-G.** Representative images showing the distribution of pSTAT3 in the ARH in adult male TanGck$^{f/f}$ (D, F) and TanGck$^{-/-}$ (E, G) mice without (D–E) or with leptin injection (F–G). **H–I.** Quantification of the number of pSTAT3-activated cells in the ARH (H) and vmARH (I) in adult male TanGck$^{f/f}$ and TanGck$^{-/-}$ mice with or without leptin injection (n = 3/3 in vehicle condition; n = 4/9 in leptin condition, respectively). ARH, arcuate nucleus; GCK, glucokinase; 3v, third ventricle. Data are means ± SEM. *p < 0.05; ***p < 0.001 compared to TanGck$^{f/f}$ group within the same metabolic condition. Scale bars: 100 μm in D-G. Refer Supplementary Figure 7.

TanGck$^{-/-}$ mice compared to TanGck$^{f/f}$ mice (Supplementary Figure 6F), suggesting an alteration in the counter-regulatory response. To further analyze glucoprivic responses in TanGck$^{-/-}$ mice, we performed 2-deoxyglucose (2-DG) injections to simulate hypoglycemia. A 2-DG injection induced lower glucagon secretion in TanGck$^{-/-}$ mice than TanGck$^{f/f}$ mice, while causing a similar increase in glucose levels (Supplementary Figure 6G–H), confirming an alteration in the counter-regulatory response. Additionally, TanGck$^{-/-}$ mice ate less following 2-DG injection compared to TanGck$^{f/f}$ mice (Supplementary Figure 6I–J) and displayed a higher drop in body and BAT temperature associated with freezing behavior (Supplementary Figure 6K-L).

3.6. Ablation of Gck-expressing tanycytes impacts arcuate neuron function

To further understand the impact of tanycyte ablation on the regulation of energy balance, we studied arcuate neuron function and physiological responses to defined imbalance conditions. Thus, we first tested the response to the anorectic leptin and orexigenic ghrelin. Following ghrelin injection, the increase in glycemia and food intake was similar in TanGck$^{f/f}$ and TanGck$^{-/-}$ mice (Figure 6A–B). In contrast, the decrease in food intake induced by leptin was lower in TanGck$^{-/-}$ mice (Figure 6C), suggesting leptin resistance. In response to leptin injection, pSTAT3 activation was lower in the ARH in TanGck$^{-/-}$ mice (Figure 6D), particularly in the vmARH (Figure 6E). As the experiment was performed in the morning when endogenous leptin levels were high, particularly in TanGck$^{-/-}$ mice (Supplementary Table 2), the vehicle condition denoted pSTAT3 activation induced by endogenous leptin. Interestingly, pSTAT3 activation was also lower in the vehicle condition (Figure 6D–E), strengthening the leptin resistance hypothesis. These defects in pSTAT3 activation in TanGck$^{-/-}$ mice occurred on the entire anteroposterior axis, although a specific subgroup of tanycytes was ablated in our model (Supplementary Figure 7A–B).

We then analyzed the short-term response to 24-h fasting. TanGck$^{-/-}$ mice ate less during short-term refeeding (Figure 7A), mainly because of the delay in meal initiation (Figure 7B). C-Fos activation was lower in the ARH in TanGck$^{-/-}$ mice after 24-h fasting (Figure 7C–E), particularly in the orexigenic NPY neurons (Figure 7F). Interestingly, this defect in c-Fos activation in TanGck$^{-/-}$ mice also occurred on the entire anteroposterior axis (Supplementary Figure 7C–E), suggesting the ablation of a restricted tanycyte subgroup that impacted the whole ARH. In the 24-h fasting condition, *Agrp* gene expression was significantly decreased in TanGck$^{-/-}$ mice, while a downward trend was evident for *Npy* expression. No changes were observed for *Pomc* or *Cart* expression mRNA (Figure 7G). With regard to tanycyte neuromodulators, the expression of *Dio2,* which is responsible for the local production of orexigenic T3 within the hypothalamus, was lower in TanGck$^{-/-}$ mice during fasting (Figure 7H).

As the decrease in food intake observed during short-term refeeding counteracts the increase in food intake observed in basal conditions, we hypothesized that these opposing phenotypes were caused by the different response timing. Food intake per period presented an upward trend in TanGck$^{-/-}$ mice that started 2-h after refeeding (Figure 7B). To further analyze this hypothesis, we performed a long-term refeeding test after 24-h fasting. Food intake progressively increased in TanGck$^{-/-}$ mice till it became significantly higher than TanGck$^{f/f}$ mice 8-h after refeeding (Figure 8A—B). C-Fos activation was higher in the ARH in TanGck$^{-/-}$ mice after 2-h-refeeding (Figure 8C—E), particularly in vmARH neurons (Figure 8F) and in NPY neurons (Figure 8G). This increase in c-Fos activation in TanGck$^{-/-}$ mice occurred on the entire anteroposterior axis (Supplementary Figure 4F—H). Interestingly, the lower c-Fos activation in the vmARH in TanGck$^{f/f}$ mice was associated with c-Fos activation in vmARH tanycytes (Figure 8C—D, H). This c-Fos activation in vmARH tanycytes significantly decreased in TanGck$^{-/-}$ mice because of tanycyte ablation (Figure 8H). No change occurred in the gene expression of orexigenic and anorexigenic neuropeptides in the mediobasal hypothalamus after 2-h refeeding (Figure 8I). Regarding the tanycyte neuromodulator, *Fgf10* mRNA was lower in TanGck$^{-/-}$ mice (Figure 8J).

4. DISCUSSION

Over the last decade, several studies established tanycytes as critical players in the regulation of energy balance, mostly because of their heterogeneity and multifunctionality. In the present study, we confirmed these peculiar tanycyte properties with regard to the expression and function of GCK. As previously reported in mice [3] and rats [9,26,27], *Gck* is weakly expressed by tanycytes along the third ventricle. While tanycytes are often categorized on the ventrodorsal axis, our neuroanatomical analysis provides a detailed description of *Gck* expression on both the ventrodorsal and anteroposterior axis and highlights an additional heterogeneity often unappreciated in the

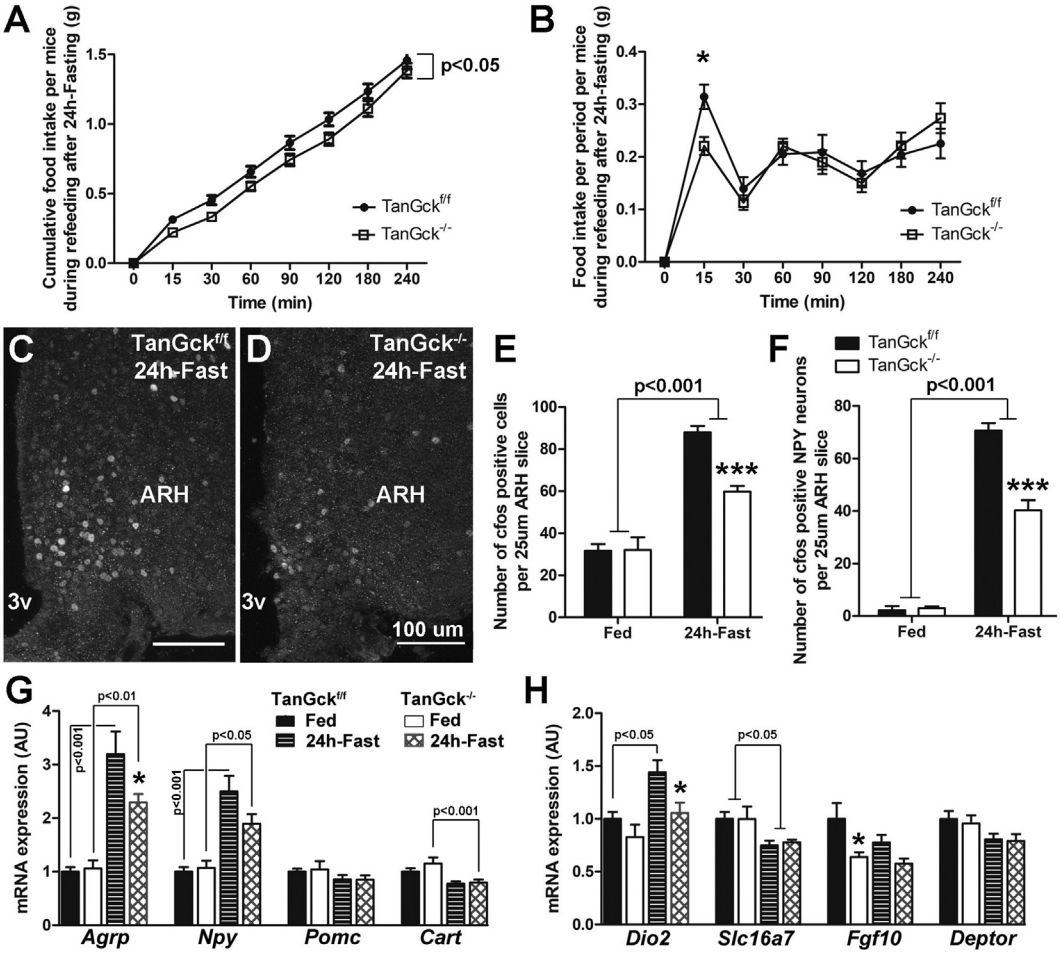

Figure 7: Tanycyte ablation induces a delay in meal initiation after fasting. **A-B.** Cumulative food intake (A) and food intake per period (B) in adult male TanGck$^{f/f}$ and TanGck$^{-/-}$ mice during 240 min refeeding after 24-h fasting (3 cohorts, n = 23/27, respectively). **C-D.** Representative images of c-Fos activity in the ARH of adult male TanGck$^{f/f}$ (C) and TanGck$^{-/-}$ (D) mice after 24-h fasting. **E-F.** Quantification of the number of c-Fos-positive cells in the ARH (E) (n = 8/6 in fed condition; 13/16 in fasted condition, respectively) and c-Fos-positive NPY neurons (F) (n = 4/4 in fed condition; 3/6 in fasted condition, respectively) in adult male TanGck$^{f/f}$ and TanGck$^{-/-}$ mice after 24-h fasting. **G-H.** Gene expression of hypothalamic neuropeptides (G) and tanycytic markers (H) in microdissected hypothalami from adult male TanGck$^{f/f}$ and TanGck$^{-/-}$ mice after 24-h fasting (n = 9/8 in fed condition; n = 15/18 in fasted condition, respectively). *Agrp*, agouti-related peptide; ARH, arcuate nucleus; *Cart*, Cocaine- and amphetamine-regulated transcript; *Dio2*, Iodothyronine Deiodinase 2; Fgf10, Fibroblast Growth Factor 10; GCK, glucokinase; *Npy*, Neuropeptide Y; *Pomc*, Pro-opiomelanocortin; Slc16a7, Monocarboxylate Transporter 2; 3v, third ventricle. Scale bars: 100 μm in C-D. Data are means ± SEM. *p < 0.05; ***p < 0.001 compared to TanGck$^{f/f}$ group within the same metabolic condition. Refer Supplementary Figure 7 and Supplementary Table 2.

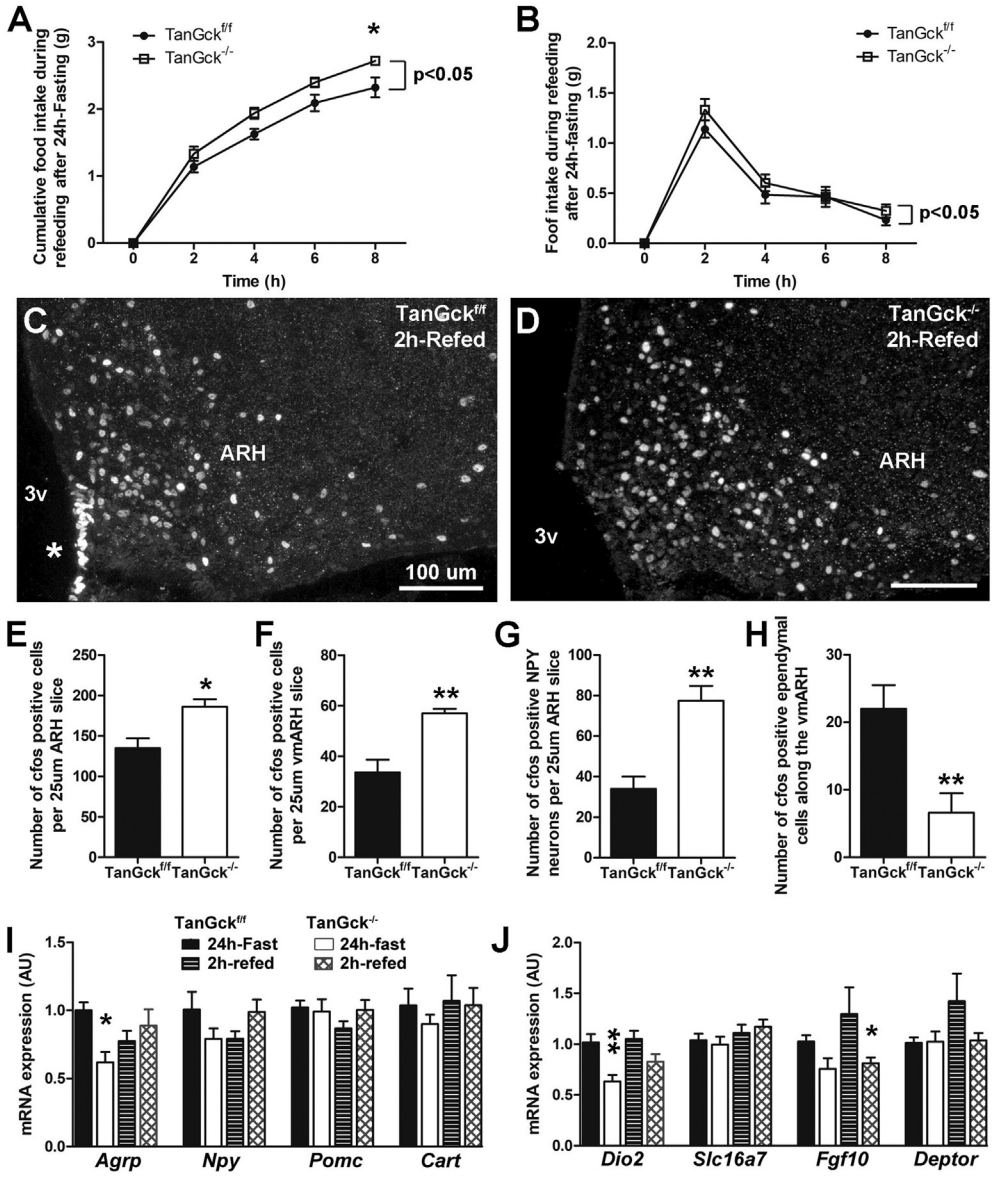

Figure 8: Tanycyte ablation induces a delay in meal termination after refeeding. **A-B.** Cumulative food intake (A) and food intake per period (B) in adult male TanGck$^{f/f}$ and TanGck$^{-/-}$ mice during 8-h refeeding after 24-h fasting (1 cohort, n = 8/7, respectively). **C-D.** Representative images of c-Fos activity in the ARH of adult male TanGck$^{f/f}$ and TanGck$^{-/-}$ mice after 2-h refeeding (asterisk = c-Fos activation in vmARH tanycytes). **E-H.** Quantification of the number of c-Fos-positive cells in the ARH (E), the vmARH (F), c-Fos-positive NPY neurons (G), and c-Fos-positive tanycytes along the vmARH (H) in adult male TanGck$^{f/f}$ and TanGck$^{-/-}$ mice after 2-h refeeding (n = 7/5, respectively). **I-J.** Gene expression of hypothalamic neuropeptides (I) and tanycytic markers (J) in microdissected hypothalami from adult male TanGck$^{f/f}$ and TanGck$^{-/-}$ mice after 2-h refeeding (n = 7/8 in fasted condition; n = 6/10 in refed condition, respectively). *Agrp*, agouti-related peptide; ARH, arcuate nucleus; *Cart*, Cocaine- and amphetamine-regulated transcript; *Dio2*, Iodothyronine Deiodinase 2; Fgf10, Fibroblast Growth Factor 10; GCK, glucokinase; *Npy*, Neuropeptide Y; *Pomc*, Pro-opiomelanocortin; Slc16a7, Monocarboxylate Transporter 2; 3v, third ventricle. Scale bars: 100 μm in C-D. Data are means ± SEM. *p < 0.05; **p < 0.01 compared to TanGck$^{f/f}$ group within the same metabolic condition. Refer to Supplementary Figure 7 and Supplementary Table 2.

literature. In particular, *Gck*-expressing tanycytes display a differential distribution along the ventricle that mostly corresponds to the ventral and dorsal β1 tanycytes in the present classification [25] but does not entirely match it, supporting the idea that tanycyte classification should be modernized [7]. Additionally, the differential distribution of *Gck*-expressing tanycytes reveals species-specificity, as *Gck*-expressing tanycytes face the entire ARH in rats [27]. In mice, *Gck*-expressing tanycytes are closely related to the lateral ME and vmARH. They are present between *bregma* −1.5 and −2.2 and absent in the posterior hypothalamus when the pituitary stalk is formed. *Gck* expression at the blood—brain interface could allow tanycytes to respond to significant variations in glucose concentration. Moreover, *Gck* expression is upregulated by refeeding, as previously reported in rats [26].

GCK is involved in numerous cellular processes that range from glycolysis to cell survival [12,13,33,34]. In tanycyte biology, the role of GCK in glucose sensing was reported *in vitro* [35] and *in vivo* [9]. In this study, GCK also appears to be involved in cell survival, as its deletion leads to tanycyte death. The ablation also concerns few tanycytes neighbors of *Gck*-expressing tanycytes, probably owing to the rupture of the ependyma. Similar phenotypes were reported in the literature

previously. GCK inhibitors, such as alloxan, induce tanycyte ablation along the ventricle in rats [8]. Similarly, streptozotocin, known to decrease *Gck* expression drastically and cause β-cell death, induces degenerative changes in the vmARH and the ME in rats because of profound alterations in tanycyte morphology [36]. In contrast, Uranga et al. did not describe changes in tanycyte morphology after using adenovirus expressing shRNA to reduce GCK levels in tanycytes [9], potentially owing to the methodological approach used in this study. In mice, the mechanisms underlying apoptosis induced by *Gck* deletion rely on the BAD signaling pathway activation in the mediobasal hypothalamus, as it has been described for other cell types [13,33,37]. However, the role of different pathways involved in tanycyte death cannot be excluded.

As *Gck*-expressing tanycytes disappear after *Gck* deletion, our approach allowed us to establish the impact of vmARH tanycyte ablation on mouse physiology. Regarding glucose homeostasis, the ablation impacts glucoprivic responses, as glucagon secretion is lower after insulin or 2-DG injection and 2-DG fails to induce food intake. Similar results were yielded in rats following tanycyte ablation by alloxan [8]. Recently, it has also been reported that tanycyte ablation impacts insulin sensitivity [38], which we did not observe with the ablation of vmARH tanycytes, suggesting that other tanycyte populations are involved in the regulation of insulin sensitivity. Regarding energy balance, the ablation of vmARH tanycytes had no clear orexigenic or anorexigenic impact. However, it leads to a complex phenotype with an increase in basal food intake and energy expenditure, and defects during energy imbalance such as a delay in meal initiation and meal termination during refeeding. Although energy expenditure also increased in these mice, the global balance shifts toward the orexigenic pathway, leading to increased adiposity. Such alterations in feeding behaviors caused by tanycytes are already documented in the literature [3,9,38–41]. A tanycyte ablation through the *Rax* promoter leads to a similar phenotype with increased adiposity correlated with an increased food intake without changes in energy expenditure [38]. Additionally, more and more studies report that tanycytes impact the morphology and function of adipose tissues [38,42]. Tanycytes notably display enrichment in genes related to the control of waist-hip ratio (WHR), an indicator of fat distribution [22]. Here, we report an alteration in BAT function, consistent with an increase in energy expenditure. While eWAT does not appear to be impacted by tanycyte function, other adipose tissue pads could be affected, such as subcutaneous WAT. Tanycytes can promote lipid mobilization and browning in subcutaneous WAT through FGF21, which results in an increase in energy expenditure and a decrease in fat accumulation [42].

With opposite physiological alterations, this complex phenotype may first rely on the loss of various tanycyte functions within the hypothalamic parenchyma. Tanycytes are glial cells that regulate energy balance positively and negatively through numerous biological functions [43]. As vmARH tanycytes are ablated in our model, all these different functions have to be considered. Here, we demonstrated the alteration of at least two main tanycyte functions, namely the regulation of blood/brain exchanges [2] and neuromodulation, in response to fuel sensing [44]. First, the tanycyte barrier and its plasticity determine hormonal and nutrient access into the mediobasal hypothalamus [2,3]. This function is notably implicated in leptin [45] and ghrelin [46] transport along with leptin sensitivity [47,48]. In our model, the tanycyte barrier is absent because of the ablation of vmARH tanycytes. It may partly explain our mouse phenotype, in particular, the deregulation in meal initiation and leptin resistance. Alternatively, tanycytes can also control brain→blood exchanges. Moreover, the β-tanycytes project to the ME fenestrated vessels to control neurosecretion, particularly that of TRH [49,50], which is involved in the control of energy expenditure [42]. However, no change appears to occur in our model. Besides blood/brain exchanges, tanycyte gliotransmission is also altered following tanycyte ablation. In this study, we report an alteration in the expression of *Dio2*. DIO2 is an enzyme specifically expressed in tanycytes in the mediobasal hypothalamus, and changes in its expression are crucial for the regulation of food intake during refeeding [28,51] and in seasonal animals [52]. DIO2 regulates the levels of orexigenic T3 in the hypothalamus that modulates NPY neuron function and energy balance [28]. Finally, the involvement of other tanycyte functions, such as stem cells or so far undescribed functions, cannot be excluded. In addition, tanycyte ablation profoundly alters the expression of *Fgf10*, which is involved in neurogenesis [53]. Despite these direct outcomes caused by the loss of tanycyte functions, we cannot exclude indirect effects because of the reorganization of the region. The destruction of the tanycyte layer in TanGck$^{-/-}$ mice led to the formation of a glial scar along the ventricle and a slight alteration in the perineuronal net in the vmARH. These modifications could also modulate arcuate neurons and play a role in the metabolic phenotype [54–56]. Finally, the destruction of the tanycyte barrier may also change the balance between central and peripheral information coming to arcuate neurons. Yoo et al. showed that the ablation of tanycytes prevents the diffusion of molecules coming from the periphery, while privileging central information [38]. This shift of balance could alter neuronal responses and the regulation of energy balance.

The last point highlighted in this study is the peculiar relationship between tanycytes and NPY neurons. Neuroanatomically, these two types of cells are connected through peculiar protrusions present along with tanycyte processes [5]. Functionally, tanycytes impact NPY neuron gene expression [9,39,57] and electrical activity [58]. In this study, the ablation of *Gck*-expressing tanycytes alters NPY neuron signaling pathway and gene expression in response to energy imbalance. Interestingly, this alteration occurs on the entire anteroposterior axis, suggesting that a restricted tanycyte subgroup may impact the entire ARH. Although tanycyte and NPY neurons appear to form functional units to regulate energy balance, their heterogeneity should not be overlooked. *Gck*-expressing tanycytes contact both GCK-positive and GCK-negative NPY neurons. These heterogeneous tanycyte/NPY neuron units could be responsible for different aspects of energy balance observed in this study, such as meal initiation [59], energy expenditure/BAT function [60], or glucoprivic responses [61].

5. CONCLUSIONS

GCK possesses numerous functions in tanycyte biology, including cell survival. The study of its distribution and its functions in tanycytes strengthens the idea that tanycytes are highly heterogeneous and multifunctional, and that their alteration may lead to intricate phenotypes that are difficult to explain. Deciphering the heterogeneity of tanycyte biology, their partnerships, and their metabolic dynamics in accordance with the physiological state of the individual will allow us to fully apprehend their role in the regulation of energy balance.

AUTHOR CONTRIBUTIONS

A.R., R.D., I.K. and R.P. performed experiments. E.C. analyzed the calorimetric data. M.B. and F.S. analyzed the single-cell RNAseq dataset. F.L. designed and performed experiments, oversaw research, analyzed data, and wrote the article. B.T edited the article.

ACKNOWLEDGMENTS

This study was supported by the Swiss National Science Foundation (PZ00P3_174120). The authors thank the CIG mouse facility (UNIL), the mouse Metabolic Evaluation Facility (MEF-UNIL), the Electron Microscopy Facility (EMF-UNIL), and the UMS2014-US41 (University of Lille) for their expert technical support. F.L. is supported by European Research Council Starting Grant (TANGO, No. 948196), Novartis Foundation for medical-biological research, and the Swiss National Science Foundation (PCEFP3_194551). F.S and M.B are supported by the Swiss National Science Foundation (310030_185292), Horizon2020 (847941), and Novartis Foundation (18A052). B.T. received support from European Research Council Advanced Grant (INTEGRATE, No. 694798) and the Swiss National Science Foundation (grant # 310030–182496).

CONFLICT OF INTEREST

The authors declare no conflict of interest.

APPENDIX A. SUPPLEMENTARY DATA

Supplementary data to this article can be found online at https://doi.org/10.1016/j.molmet.2021.101311.

REFERENCES

[1] Sohn, J.-W., 2015. Network of hypothalamic neurons that control appetite. BMB Reports 48(4):229–233. https://doi.org/10.5483/BMBRep.2015.48.4.272.

[2] Langlet, F., 2014. Tanycytes: a gateway to the metabolic hypothalamus. Journal of Neuroendocrinology 26(11):753–760. https://doi.org/10.1111/jne.12191.

[3] Langlet, F., Levin, B.E., Luquet, S., Mazzone, M., Messina, A., Dunn-Meynell, A.A., et al., 2013. Tanycytic VEGF-A boosts blood-hypothalamus barrier plasticity and access of metabolic signals to the arcuate nucleus in response to fasting. Cell Metabolism 17(4):607–617. https://doi.org/10.1016/j.cmet.2013.03.004.

[4] Mullier, A., Bouret, S.G., Prevot, V., Dehouck, B., 2010. Differential distribution of tight junction proteins suggests a role for tanycytes in blood-hypothalamus barrier regulation in the adult mouse brain. The Journal of Comparative Neurology 518(7):943–962. https://doi.org/10.1002/cne.22273.

[5] Pasquettaz, R., Kolotuev, I., Rohrbach, A., Gouelle, C., Pellerin, L., Langlet, F., 2020. Peculiar protrusions along tanycyte processes face diverse neural and non-neural cell types in the hypothalamic parenchyma. The Journal of Comparative Neurology. https://doi.org/10.1002/cne.24965.

[6] Frayling, C., Britton, R., Dale, N., 2011. ATP-mediated glucosensing by hypothalamic tanycytes. The Journal of Physiology 589(Pt 9):2275–2286. https://doi.org/10.1113/jphysiol.2010.202051.

[7] Langlet, F., 2019. Tanycyte gene expression dynamics in the regulation of energy homeostasis. Frontiers in Endocrinology 10:286. https://doi.org/10.3389/fendo.2019.00286.

[8] Sanders, N.M., Dunn-Meynell, A.A., Levin, B.E., 2004. Third ventricular alloxan reversibly impairs glucose counterregulatory responses. Diabetes 53(5):1230–1236.

[9] Uranga, R.M., Millán, C., Barahona, M.J., Recabal, A., Salgado, M., Martinez, F., et al., 2017. Adenovirus-mediated suppression of hypothalamic glucokinase affects feeding behavior. Scientific Reports 7(1):3697. https://doi.org/10.1038/s41598-017-03928-x.

[10] Postic, C., Shiota, M., Niswender, K.D., Jetton, T.L., Chen, Y., Moates, J.M., et al., 1999. Dual roles for glucokinase in glucose homeostasis as determined by liver and pancreatic β cell-specific gene knock-outs using Cre recombinase. Journal of Biological Chemistry 274(1):305–315. https://doi.org/10.1074/jbc.274.1.305.

[11] Langlet, F., Haeusler, R.A., Lindén, D., Ericson, E., Norris, T., Johansson, A., et al., 2017. Selective inhibition of FOXO1 activator/repressor balance modulates hepatic glucose handling. Cell 171(4):824–835. https://doi.org/10.1016/j.cell.2017.09.045 e18.

[12] Matschinsky, F.M., Wilson, D.F., 2019. The central role of glucokinase in glucose homeostasis: a perspective 50 Years after demonstrating the presence of the enzyme in islets of langerhans. Frontiers in Physiology 10:148. https://doi.org/10.3389/fphys.2019.00148.

[13] Kim, W.-H., Lee, J.W., Suh, Y.H., Hong, S.H., Choi, J.S., Lim, J.H., et al., 2005. Exposure to chronic high glucose induces beta-cell apoptosis through decreased interaction of glucokinase with mitochondria: downregulation of glucokinase in pancreatic beta-cells. Diabetes 54(9):2602–2611. https://doi.org/10.2337/diabetes.54.9.2602.

[14] Steinbusch, L.K.M., Picard, A., Bonnet, M.S., Basco, D., Labouèbe, G., Thorens, B., 2016. Sex-specific control of fat mass and counterregulation by hypothalamic glucokinase. Diabetes 65(10):2920–2931. https://doi.org/10.2337/db15-1514.

[15] Shimshek, D.R., Kim, J., Hübner, M.R., Spergel, D.J., Buchholz, F., Casanova, E., et al., 2002. Codon-improved Cre recombinase (iCre) expression in the mouse. Genesis (New York, N.Y.) 32(1):19–26. https://doi.org/10.1002/gene.10023, 2000.

[16] Langlet, F., 2020. Targeting tanycytes: balance between efficiency and specificity. Neuroendocrinology 110(7–8):574–581. https://doi.org/10.1159/000505549.

[17] Kolotuev, I., Schwab, Y., Labouesse, M., 2009. A precise and rapid mapping protocol for correlative light and electron microscopy of small invertebrate organisms. Biology of the Cell 102(2):121–132. https://doi.org/10.1042/BC20090096.

[18] Kolotuev, I., 2014. Positional correlative anatomy of invertebrate model organisms increases efficiency of TEM data production. Microscopy and Microanalysis: The Official Journal of Microscopy Society of America, Microbeam Analysis Society, Microscopical Society of Canada 20(5):1392. https://doi.org/10.1017/S1431927614012999. –403.

[19] Langlet, F., Mullier, A., Bouret, S.G., Prevot, V., Dehouck, B., 2013. Tanycyte-like cells form a blood-cerebrospinal fluid barrier in the circumventricular organs of the mouse brain. The Journal of Comparative Neurology 521(15):3389–3405. https://doi.org/10.1002/cne.23355.

[20] Burel, A., Lavault, M.-T., Chevalier, C., Gnaegi, H., Prigent, S., Mucciolo, A., et al., 2018. A targeted 3D EM and correlative microscopy method using SEM array tomography. Development 145(12). https://doi.org/10.1242/dev.160879.

[21] Luse, S.A., 1956. Electron microscopic observations of the central nervous system. The Journal of Biophysical and Biochemical Cytology 2(5):531–542.

[22] Campbell, J.N., Macosko, E.Z., Fenselau, H., Pers, T.H., Lyubetskaya, A., Tenen, D., et al., 2017. A molecular census of arcuate hypothalamus and median eminence cell types. Nature Neuroscience 20(3):484–496. https://doi.org/10.1038/nn.4495.

[23] Hao, Y., Hao, S., Andersen-Nissen, E., Mauck, W.M., Zheng, S., Butler, A., et al., 2021. Integrated analysis of multimodal single-cell data. Cell 184(13):3573–3587. https://doi.org/10.1016/j.cell.2021.04.048 e29.

[24] Tschöp, M.H., Speakman, J.R., Arch, J.R.S., Auwerx, J., Brüning, J.C., Chan, L., et al., 2012. A guide to analysis of mouse energy metabolism. Nature Methods 9(1):57–63. https://doi.org/10.1038/nmeth.1806.

[25] Akmayev, I.G., Popov, A.P., 1977. Morphological aspects of the hypothalamic-hypophyseal system. VII. The tanycytes: their relation to the hypophyseal adrenocorticotrophic function. An ultrastructural study. Cell and Tissue Research 180(2):263–282.

[26] Salgado, M., Tarifeño-Saldivia, E., Ordenes, P., Millán, C., Yañez, M.J., Llanos, P., et al., 2014. Dynamic localization of glucokinase and its regulatory protein in hypothalamic tanycytes. PloS One 9(4):e94035. https://doi.org/10.1371/journal.pone.0094035.

[27] Millán, C., Martínez, F., Cortés-Campos, C., Lizama, I., Yañez, M.J., Llanos, P., et al., 2010. Glial glucokinase expression in adult and post-natal development of the hypothalamic region. ASN Neuro 2(3):e00035. https://doi.org/10.1042/AN20090059.

[28] Coppola, A., Liu, Z.-W., Andrews, Z.B., Paradis, E., Roy, M.-C., Friedman, J.M., et al., 2007. A central thermogenic-like mechanism in feeding regulation: an interplay between arcuate nucleus T3 and UCP2. Cell Metabolism 5(1):21—33. https://doi.org/10.1016/j.cmet.2006.12.002.

[29] Saraste, A., Pulkki, K., 2000. Morphologic and biochemical hallmarks of apoptosis. Cardiovascular Research 45(3):528—537. https://doi.org/10.1016/S0008-6363(99)00384-3.

[30] Danial, N.N., Gramm, C.F., Scorrano, L., Zhang, C.-Y., Krauss, S., Ranger, A.M., et al., 2003. BAD and glucokinase reside in a mitochondrial complex that integrates glycolysis and apoptosis. Nature 424(6951):952—956. https://doi.org/10.1038/nature01825.

[31] Wei, P., Shi, M., Barnum, S., Cho, H., Carlson, T., Fraser, J.D., 2009. Effects of glucokinase activators GKA50 and LY2121260 on proliferation and apoptosis in pancreatic INS-1 beta cells. Diabetologia 52(10):2142—2150. https://doi.org/10.1007/s00125-009-1446-0.

[32] Kim, W.-H., Lee, J.W., Suh, Y.H., Lee, H.J., Lee, S.H., Oh, Y.K., et al., 2007. AICAR potentiates ROS production induced by chronic high glucose: roles of AMPK in pancreatic beta-cell apoptosis. Cellular Signalling 19(4):791—805. https://doi.org/10.1016/j.cellsig.2006.10.004.

[33] Marqués, P., Kamitz, A., Bartolomé, A., Burillo, J., Martínez, H., Jiménez, B., et al., 2019. Essential role of glucokinase in the protection of pancreatic β cells to the glucose energetic status. Cell Death Discovery 5:138. https://doi.org/10.1038/s41420-019-0219-x.

[34] Shirakawa, J., Togashi, Y., Sakamoto, E., Kaji, M., Tajima, K., Orime, K., et al., 2013. Glucokinase activation ameliorates ER stress—induced apoptosis in pancreatic β-cells. Diabetes 62(10):3448—3458. https://doi.org/10.2337/db13-0052.

[35] Orellana, J.A., Sáez, P.J., Cortés-Campos, C., Elizondo, R.J., Shoji, K.F., Contreras-Duarte, S., et al., 2012. Glucose increases intracellular free Ca(2+) in tanycytes via ATP released through connexin 43 hemichannels. Glia 60(1):53—68. https://doi.org/10.1002/glia.21246.

[36] Bestetti, G., Rossi, G.L., 1983. Hypothalamic lesions associated with streptozotocin diabetes, rat. In: Jones, T.C., Mohr, U., Hunt, R.D., Capen, C.C. (Eds.), Endocrine system. Berlin, Heidelberg: Springer. p. 331. —8.

[37] Danial, N.N., Walensky, L.D., Zhang, C.-Y., Choi, C.S., Fisher, J.K., Molina, A.J.A., et al., 2008. Dual role of proapoptotic BAD in insulin secretion and beta cell survival. Nature Medicine 14(2):144—153. https://doi.org/10.1038/nm1717.

[38] Yoo, S., Cha, D., Kim, S., Jiang, L., Cooke, P., Adebesin, M., et al., 2020. Tanycyte ablation in the arcuate nucleus and median eminence increases obesity susceptibility by increasing body fat content in male mice. Glia 68(10):1987—2000. https://doi.org/10.1002/glia.23817.

[39] Barahona, M.J., Llanos, P., Recabal, A., Escobar-Acuña, K., Elizondo-Vega, R., Salgado, M., et al., 2018. Glial hypothalamic inhibition of GLUT2 expression alters satiety, impacting eating behavior. Glia 66(3):592—605. https://doi.org/10.1002/glia.23267.

[40] Elizondo-Vega, R., Cortés-Campos, C., Barahona, M.J., Carril, C., Ordenes, P., Salgado, M., et al., 2016. Inhibition of hypothalamic MCT1 expression increases food intake and alters orexigenic and anorexigenic neuropeptide expression. Scientific Reports 6:33606. https://doi.org/10.1038/srep33606.

[41] Kim, S., Kim, N., Park, S., Jeon, Y., Lee, J., Yoo, S.-J., et al., 2019. Tanycytic TSPO inhibition induces lipophagy to regulate lipid metabolism and improve energy balance. Autophagy, 1—21. https://doi.org/10.1080/15548627.2019.1659616.

[42] Geller, S., Arribat, Y., Netzahualcoyotzi, C., Lagarrigue, S., Carneiro, L., Zhang, L., et al., 2019. Tanycytes regulate lipid homeostasis by sensing free fatty acids and signaling to key hypothalamic neuronal populations via FGF21 secretion. Cell Metabolism. https://doi.org/10.1016/j.cmet.2019.08.004.

[43] Prevot, V., Dehouck, B., Sharif, A., Ciofi, P., Giacobini, P., Clasadonte, J., 2018. The versatile tanycyte: a hypothalamic integrator of reproduction and energy metabolism. Endocrine Reviews 39(3):333—368. https://doi.org/10.1210/er.2017-00235.

[44] Clasadonte, J., Prevot, V., 2018. The special relationship: glia-neuron interactions in the neuroendocrine hypothalamus. Nature Reviews Endocrinology 14(1):25—44. https://doi.org/10.1038/nrendo.2017.124.

[45] Balland, E., Dam, J., Langlet, F., Caron, E., Steculorum, S., Messina, A., et al., 2014. Hypothalamic tanycytes are an ERK-gated conduit for leptin into the brain. Cell Metabolism 19(2):293—301. https://doi.org/10.1016/j.cmet.2013.12.015.

[46] Collden, G., Balland, E., Parkash, J., Caron, E., Langlet, F., Prevot, V., et al., 2015. Neonatal overnutrition causes early alterations in the central response to peripheral ghrelin. Molecular Metabolism 4(1):15—24. https://doi.org/10.1016/j.molmet.2014.10.003.

[47] Guillebaud, F., Girardet, C., Abysique, A., Gaigé, S., Barbouche, R., Verneuil, J., et al., 2017. Glial endozepines inhibit feeding-related autonomic functions by acting at the brainstem level. Frontiers in Neuroscience 11. https://doi.org/10.3389/fnins.2017.00308.

[48] Jiang, H., Gallet, S., Klemm, P., Scholl, P., Folz-Donahue, K., Altmüller, J., et al., 2020. MCH neurons regulate permeability of the median eminence barrier. Neuron. https://doi.org/10.1016/j.neuron.2020.04.020.

[49] Müller-Fielitz, H., Stahr, M., Bernau, M., Richter, M., Abele, S., Krajka, V., et al., 2017. Tanycytes control the hormonal output of the hypothalamic-pituitary-thyroid axis. Nature Communications 8(1):484. https://doi.org/10.1038/s41467-017-00604-6.

[50] Farkas, E., Varga, E., Kovács, B., Szilvásy-Szabó, A., Cote-Vélez, A., Péterfi, Z., et al., 2020. A glial-neuronal circuit in the median eminence regulates thyrotropin-releasing hormone-release via the endocannabinoid system. IScience 23(3):100921. https://doi.org/10.1016/j.isci.2020.100921.

[51] Diano, S., Naftolin, F., Goglia, F., Horvath, T.L., 1998. Fasting-induced increase in type II iodothyronine deiodinase activity and messenger ribonucleic acid levels is not reversed by thyroxine in the rat hypothalamus. Endocrinology 139(6):2879—2884. https://doi.org/10.1210/endo.139.6.6062.

[52] Petri, I., Diedrich, V., Wilson, D., Fernández-Calleja, J., Herwig, A., Steinlechner, S., et al., 2016. Orchestration of gene expression across the seasons: hypothalamic gene expression in natural photoperiod throughout the year in the Siberian hamster. Scientific Reports 6(1):29689. https://doi.org/10.1038/srep29689.

[53] Haan, N., Goodman, T., Najdi-Samiei, A., Stratford, C.M., Rice, R., El Agha, E., et al., 2013. Fgf10-expressing tanycytes add new neurons to the appetite/energy-balance regulating centers of the postnatal and adult hypothalamus. Journal of Neuroscience: The Official Journal of the Society for Neuroscience 33(14):6170—6180. https://doi.org/10.1523/JNEUROSCI.2437-12.2013.

[54] Yang, L., Qi, Y., Yang, Y., 2015. Astrocytes control food intake by inhibiting AGRP neuron activity via adenosine A1 receptors. Cell Reports 11(5):798—807. https://doi.org/10.1016/j.celrep.2015.04.002.

[55] Mirzadeh, Z., Alonge, K.M., Cabrales, E., Herranz-Pérez, V., Scarlett, J.M., Brown, J.M., et al., 2019. Perineuronal net formation during the critical period for neuronal maturation in the hypothalamic arcuate nucleus. Nature Metabolism 1(2):212—221. https://doi.org/10.1038/s42255-018-0029-0.

[56] Alonge, K.M., Mirzadeh, Z., Scarlett, J.M., Logsdon, A.F., Brown, J.M., Cabrales, E., et al., 2020. Hypothalamic perineuronal net assembly is required for sustained diabetes remission induced by fibroblast growth factor 1 in rats.

Nature Metabolism 2(10):1025—1033. https://doi.org/10.1038/s42255-020-00275-6.

[57] Böttcher, M., Müller-Fielitz, H., Sundaram, S.M., Gallet, S., Neve, V., Shionoya, K., et al., 2020. NF-κB signaling in tanycytes mediates inflammation-induced anorexia. Molecular Metabolism, 101022. https://doi.org/10.1016/j.molmet.2020.101022.

[58] Bolborea, M., Pollatzek, E., Benford, H., Sotelo-Hitschfeld, T., Dale, N., 2020. Hypothalamic tanycytes generate acute hyperphagia through activation of the arcuate neuronal network. Proceedings of the National Academy of Sciences of the United States of America. https://doi.org/10.1073/pnas.1919887117.

[59] Wu, Q., Howell, M.P., Cowley, M.A., Palmiter, R.D., 2008. Starvation after AgRP neuron ablation is independent of melanocortin signaling. Proceedings of the National Academy of Sciences of the United States of America 105(7): 2687—2692. https://doi.org/10.1073/pnas.0712062105.

[60] Shi, Y.-C., Lau, J., Lin, Z., Zhang, H., Zhai, L., Sperk, G., et al., 2013. Arcuate NPY controls sympathetic output and BAT function via a relay of tyrosine hydroxylase neurons in the PVN. Cell Metabolism 17(2):236—248. https://doi.org/10.1016/j.cmet.2013.01.006.

[61] Luquet, S., Phillips, C.T., Palmiter, R.D., 2007. NPY/AgRP neurons are not essential for feeding responses to glucoprivation. Peptides 28(2):214—225. https://doi.org/10.1016/j.peptides.2006.08.036.

